THREE-DIMENSIONAL WIND MEASUREMENTS AND MODELING USING A BI-STATIC FABRY-PEROT INTERFEROMETER SYSTEM IN BRAZIL

BY

DANIEL J. FISHER

THESIS

Submitted in partial fulfillment of the requirements
for the degree of Master of Science in Electrical and Computer Engineering
in the Graduate College of the
University of Illinois at Urbana-Champaign, 2013

Urbana, Illinois

Adviser:

Associate Professor Jonathan J. Makela

ABSTRACT

The earth's upper atmosphere has been studied for over a century now, and while a multitude of data has been collected studying the plasma in the ionosphere, there are not equivalent amounts of data on neutrals in the thermosphere to pair with these plasma observations. The Remote Equatorial Nighttime Observatory for Ionospheric Regions (RENOIR) project consists of two observing systems stationed in northeastern Brazil in Cajazeiras (6.87°S, 38.56°W) and Cariri (7.38°S, 36.52°W) since 2009. They are separated by 232.28 km and each is equipped with a Fabry-Perot interferometer (FPI) to measure neutral wind velocities and neutral temperatures using observations of the 630.0-nm emission caused by the dissociative recombination of O_2^+. The FPI systems can operate in two different modes: cardinal and common volume (CV). In cardinal mode, each FPI looks at a 45° elevation angle towards geographic north, east, south, and west followed by a zenith and laser image. In common volume mode, the two FPIs are synchronized to observe three common locations followed by both a zenith and laser observation. Two common volume points, one to the north and one to the south, are where the two FPIs have the same elevation angle but are looking orthogonal to one another in the horizontal plane. The third point is an inline measurement to the midpoint of the two sites. Vector neutral winds in the horizontal plane can be computed at the two common volume points, and a vertical neutral wind can be found at the inline point.

FPIs are phase-based instruments, meaning a zero-reference is needed in order to get an absolute wind measurement. Since there is no practical 630.0-nm lab source, the zero-Doppler source is typically obtained from the zenith airglow measurements because the vertical winds are assumed to be zero across the night. However, the inline zenith measurements give non-zero winds under this assumption, consequently contradicting it. Therefore, the observations of the frequency-stabilized HeNe laser are used as a zero-Doppler reference to improve the derived vertical and horizontal neutral winds. This thesis validates this new technique by both developing an analytical model for the CV winds and by confirming it with results from actual observations made in Brazil.

To the poor, future graduate student who reads this... I'm sorry.
I sincerely hope this thesis helps you understand just one thing a bit better.
Just keep swimming!

ACKNOWLEDGMENTS

First of all, I would like to thank my advisor, Jonathan Makela, for having the patience to keep me as his grad student, all the while supporting and guiding me. He continues to make my graduate experience better than I could have hoped. I must acknowledge Ricardo Buriti and Rafael Mesquita, who have made sure my adventures fixing the Brazilian equipment went as smoothly as possible. I'd like to thank my family, who have been an excellent motivation throughout my entire life. Also, I need to thank my friends, who have kept me sane in school and still encouraged me to keep going; it has been a religious experience. Finally, thanks to my fellow graduate students in the Remote Sensing and Space Sciences group at Illinois who have been a part of this experience: Tim Duly, Thomas Gehrels, Brian Harding, Yiyi Huang, Uday Kanwar, Tony Mangognia, Ethan Miller, Peter Hedlund, and Pablo Reyes.

TABLE OF CONTENTS

LIST OF TABLES

LIST OF FIGURES

LIST OF ABBREVIATIONS

CAJ	Cajazeiras, Brazil
CAR	Cariri, Brazil
CV	Common Volume
CVN	Common Volume North
CVS	Common Volume South
EPB	Equatorial Plasma Bubble
EUV	Extreme Ultraviolet
FOV	Field-of-View
FPI	Fabry-Perot Interferometer
FSR	Free Spectral Range
FWHM	Full-Width at Half-Max
GNSS	Global Navigation Satellite Systems
GPS	Global Positioning Systems
HCL	Hollow Cathode Lamp
HWM	Horizontal Wind Model
IN	Common Volume Inline
LM	Levenberg-Marquardt
LOS	Line-of-Sight
LT	Local Time
MSIS	Mass Spectrometer and Incoherent Scatter Model

MTM	Midnight Temperature Maximum
NATION	North American Thermosphere Ionopshere Observing Network
NIR	Near-Infrared
RENOIR	Remote Equatorial Nighttime Observatory for Ionospheric Regions
SNR	Signal-to-Noise Ratio
TEC	Total Electron Content
TIE-GCM	Thermosphere-Ionosphere Electrodynamics General Circulation Model
UT	Universal Time (Greenwich Meridian Time)
UV	Ultraviolet
WAM	Whole Atmosphere Model

CHAPTER 1

MOTIVATION

Many types of instruments have been used to measure and quantify the properties of the upper atmosphere. From imaging systems, Fabry-Perot interferometers (FPIs), global positioning system (GPS) receivers, radars, and magnetometers, scientists have been searching to understand the complex interaction between the earth and space. In the past few decades, instrumentation has improved a great deal, and more sites spread around the globe are being used to uncover the mysteries of the atmosphere. At the same time, there are a growing number of users of global navigation satellite systems (GNSS), communication satellites, and other technologies that can be affected by the state of the upper atmosphere. This growth of technology means more humans stand to be affected by space weather; the power grid, radar signals, long-distance communication systems, satellites, and astronauts all can be disturbed or harmed by solar storms. In order to observe such disturbances (and ultimately understand and correctly predict them), it is important to be constantly observing our atmosphere. Scientists have been compiling data from various instruments both in space and around the globe in order to accurately model the upper atmosphere in terms of particle concentrations, temperature, winds, and drifts. These models are still far from perfect; if storm forecasting is desired, modelers need more data collected by instruments with desired spatial and temporal resolutions. Through the understanding of the earth's upper atmosphere, scientists hope to fully comprehend the complex space–earth environment and engineers can design satellites and power equipment that are less affected by storms.

A bi-static FPI system has been operating in northeastern Brazil since 2009 to measure the 630.0-nm redline emission of the ionospheric F layer. From a series of cardinal measurements, we derive the equatorial neutral temperature and geographic neutral winds using the assumption that there is no vertical wind throughout the night. This assumption is necessary because the winds are calculated from a Doppler shift and there is no reasonable zero-Doppler reference for the 630.0-nm wavelength. The Brazilian system has the added capability of deducing both vertical winds and horizontal vector winds when coordinating the two FPIs to run in a truly bi-static common volume mode. When this mode is configured, our analysis produces non-zero vertical winds at night, specifically at dusk. This finding agrees with those from other interferometer and non-interferometer based neutral wind measurements ([1], [2], [3], and [4]). Thus a new zero-Doppler technique is needed such that there are no contradictions between assumptions and measurements. Such improved measurements would help elucidate the complex physics of the nighttime F-region dynamo in this region; the neutral wind is the major driving force behind the F-region dynamo.

These data are also useful for comparisons with global temperature and wind models, such as MSIS, HWM, and WAM ([5], [6], and [7], respectively). Since neutral wind and temperature data are fairly sparse, empirical models can be improved by including this dataset into their algorithms. For empirical and physics-based models, our dataset can be used as a means of verification. Figures 1.1 and 1.2 show an example of this validation for zonal winds from Horizontal Wind Model '07 (HWM07 [8]). Figure 1.1 shows approximately three years of zonal wind data collected from the RENOIR FPIs. Figure 1.2 shows the zonal wind output of HWM07 for the same date range and times. Note that the model is not perfect; in fact, it seems to be lacking the diurnal component seen in our data. Clearly, the Brazilian sector is under-represented in the models, and the inclusion of our data can help correct these disagreements.

In this thesis, the bi-static FPI system and operations will be described. Using these measurements in a specific viewing geometry, where both FPIs look at a common volume of sky, we will show how vector horizontal wind fields and vertical wind measurements are obtained using observations of the 630.0-nm nightglow emission. Then a series of zero-reference techniques will be compared both theoretically and with actual data from the sites when the FPIs are set to scan in this common volume mode. Finally, we study the accuracy of calculated three-dimensional neutral winds through analytical models and results from actual observations made in Brazil.

To begin, Chapter 2 examines the basic characteristics of the ionosphere. Chapter 3 covers the current instrumentation we have deployed in Brazil

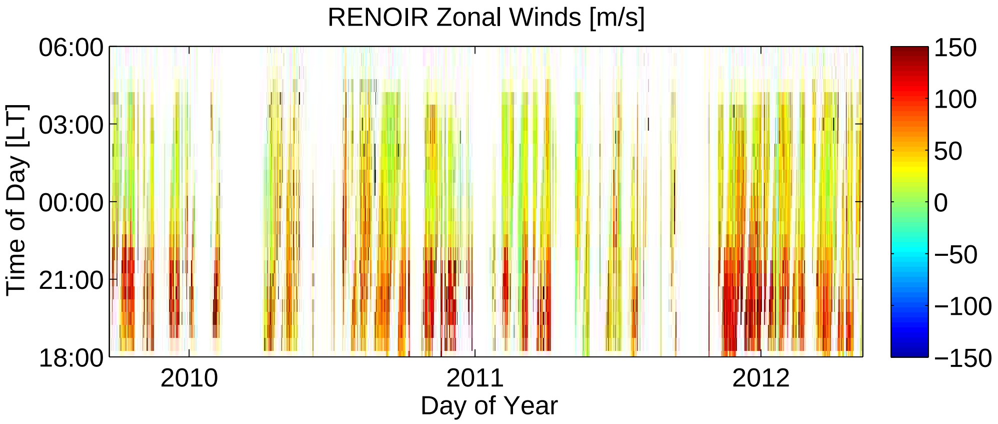

Figure 1.1: Approximately three years of zonal wind data from RENOIR.

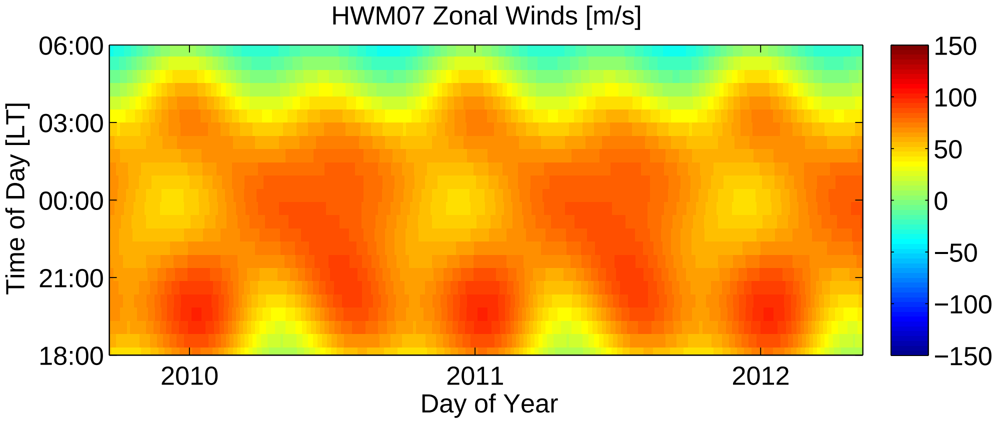

Figure 1.2: Corresponding HWM07 output for zonal winds in Brazil.

to study the temperature and velocities of the neutrals at 250-km altitude. Chapter 4 describes the three techniques used to analyze the FPI data and accurately compute three-dimensional winds. Chapter 5 details our simulation and results using the bi-static method to scan the skies. Finally, Chapter 6 presents a conclusion of this work along with a discussion of future work for this and other projects.

CHAPTER 2

INTRODUCTION

This chapter introduces some background covering the earth's ionosphere to give a basis for the science described in further chapters. It provides an overview of the upper atmosphere by describing the chemistry, the electromagnetic dynamo, and the solar influence on the thermosphere with an emphasis on the contributions that relate to the measured 630.0-nm emission.

2.1 The Upper Atmosphere

The ionosphere is the region of the atmosphere from about 90 to 1000 km in altitude where there is a large concentration of plasma, or free ions and electrons. This region is collocated with the neutral atmosphere which is stratified by temperature. The troposphere is the layer starting at the surface and extending upwards where the temperature decreases as altitude increases. The stratosphere is above this layer and is where the temperature starts increasing as altitude increases due to photon absorption by ozone. The following layer, the mesosphere, returns to a decrease in temperature with increase in height. The final layer is the thermosphere where once again temperature increases with altitude due to incoming high energy solar radiation. The ionosphere is coincident with the mesosphere and thermosphere.

The vertical structure of the ionosphere is typically divided into regions by the properties of the plasma density. First, note that the neutral density increases exponentially as altitude decreases due to earth's gravity pulling more mass towards itself. Second, solar energy decreases as altitude decreases due to higher absorption and reflections from the increase of neutral constituents. Simply, there are many particles near the surface but less radiation to ionize them, while there are fewer particles towards space with excessive radiation for ionizing them. Therefore, a peak concentration of ions forms somewhere

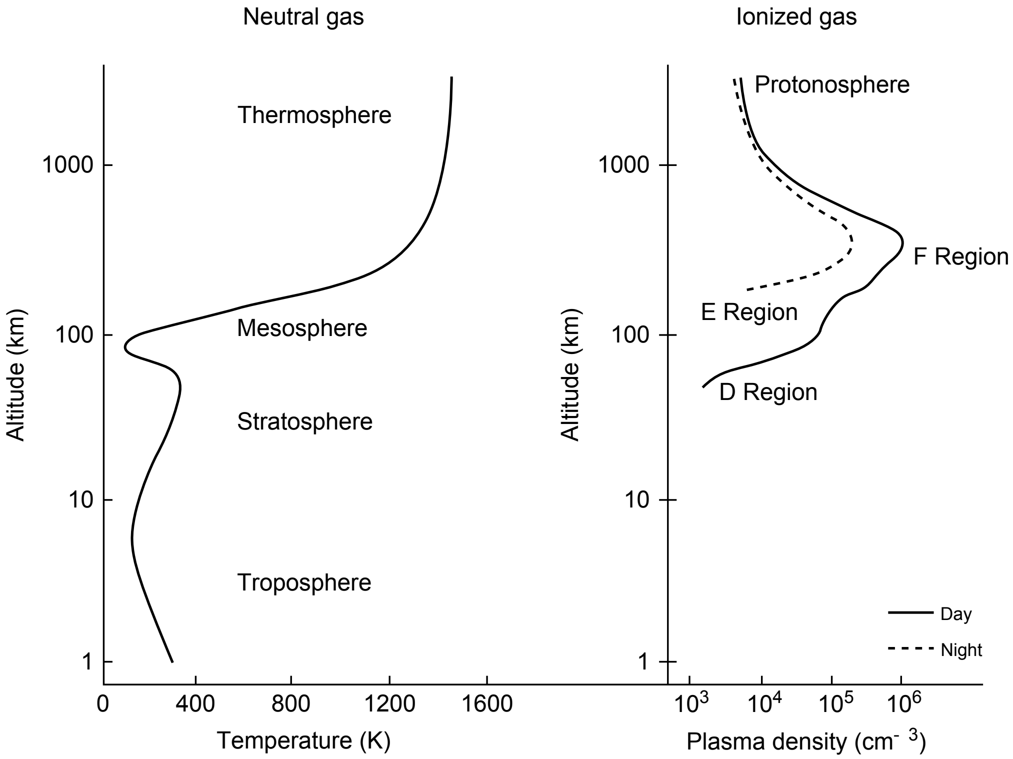

Figure 2.1: Profile of the temperature (left) and plasma density (right) of the earth's atmosphere. Reprinted from The Earth's Ionosphere, Kelley, Page 5, 1989, with permission from Elsevier [9].

in between. The peak at 350 km has been labeled the *F* region, while a secondary peak at 95 km has been labeled the *E* region. These two regions span roughly 150 to 500 km and 90 to 150 km in altitude, respectively. A *D* region also exists below 90 km in a thin layer that only exists in the daylight. Note that only the *F* region does not completely recombine and vanish during the nighttime. Figure 2.1 gives a typical profile of the neutral temperature and ion density.

2.2 Airglow Chemistry

Many chemical interactions happen in the atmosphere, all of which transfer energy in one form or another; some transfer momentum, others radiate. Certain reactions are luminescent, where a chemical reaction or photon absorption causes a molecule to release the excess energy in the form of light [10]. One well-known observable chemiluminescent reaction is the aurora bo-

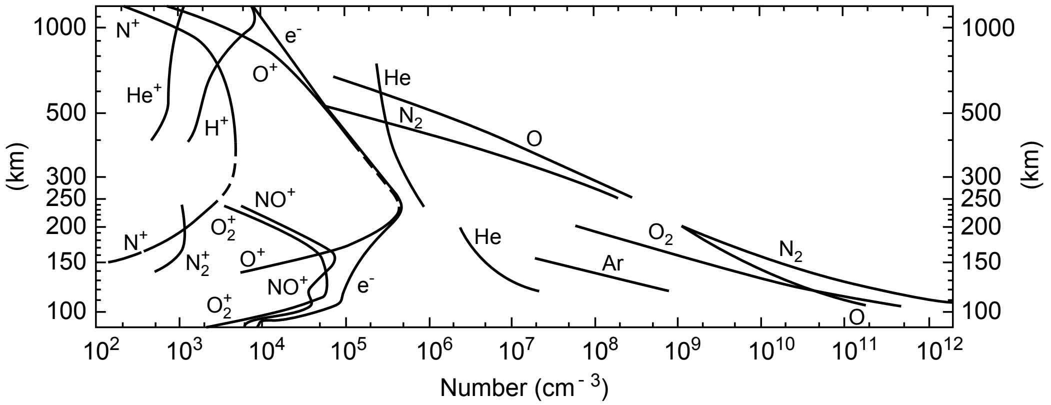

Figure 2.2: Daytime concentration of atmospheric constituents. Reprinted from The Earth's Ionosphere, Kelley, Page 6, 1989, with permission from Elsevier [9].

realis, or northern lights. While this phenomenon is very bright, it typically takes place in the polar regions. In order to learn about the ionosphere in the low and mid-latitudes through passive imaging, another "glowing" emission must be used. These reactions are often referred to as airglow.

On the earth's surface, dry air consists of 78% N_2, 21% O_2, and 1% other gases, which are all very well mixed together [11]. Above 120 km, O and O_2 are found in equal concentration and, above 250 km, atomic oxygen becomes the dominant species in the atmosphere [9], as seen in Figure 2.2. The main ion concentrations around 250 km (the *F* region) are e^- and O^+ which are created from the photo-dissociation of the oxygen atom by UV radiation. Oxygen, conveniently abundant at ionospheric altitudes, also happens to play an important role in creating specific airglow emissions.

Oxygen is involved in the emission of three commonly used airglow lines, 557.7 nm, 630.0 nm, and 777.4 nm. The 557.7-nm greenline emission is a bright, short-lived reaction (250 Rayleighs, 0.74-s lifetime) but occurs in the mesosphere, below the region of interest for this work [12]. The 777.4 nm NIR emission is due to the radiative recombination of ionized oxygen and is described by the following reaction [9]:

$$\mathrm{O}^+ + e^- \to \mathrm{O} + hv. \tag{2.1}$$

Although the emission occurs quickly compared to the 110-s lifetime of the 630.0-nm emission, its brightness is much dimmer, and the reaction occurs with plasmas only (no neutral winds measured). Thus, the 630.0-nm redline emission is chosen to study the neutral thermosphere/ionosphere. The 630.0-nm emission is produced through the dissociative recombination of O_2^+ [13]:

$$O_2^+ + e^- \rightarrow 2O(^1S,^1D,^3P). \tag{2.2}$$

The $O(^1D)$ excited state, which emits the 630.0-nm photon, is created in a fraction of the time it takes for the O_2^+ to form. The production of O_2^+ is the limiting reactant of this system. It is produced through an ion exchange with an ionized oxygen atom:

$$O_2 + O^+ \rightarrow O_2^+ + O. \tag{2.3}$$

There are also three reactions that cause the $O(^1D)$ to be depleted before emitting a photon:

$$\begin{aligned} O(^1D) + N_2 &\rightarrow O(^3P) + N_2 \\ O(^1D) + O_2 &\rightarrow O(^3P) + O_2 \\ O(^1D) &\rightarrow O(^3P) + hv. \end{aligned} \tag{2.4}$$

The first two are known as quenching reactions while the latter is spontaneous recombination. The total estimated intensity of the nighttime redline emission is on the order of 100 Rayleighs, which can be calculated from the volume emission rate [14]:

$$k_{6300} = \frac{0.76 A_{1_D} \beta_1 k_1 [O^+][O_2]}{A_{1_D} + k_3[N_2] + k_4[O_2] + k_5[e^-]}. \tag{2.5}$$

The coefficients for the 630.0-nm reaction are in presented in Table 2.1. The 630.0-nm emission rate shows that it is affected by both plasma and neutral conditions in the F region. The redline emission peaks at roughly 250 km due to the balance between ion and neutral concentrations, in the same sense as the ionosphere forms due to a balance between solar energy and particle density. If the plasma density decreases in the ionosphere, the decreased concentration of electrons and O^+ ions decreases the emission rate. Less signal intensity could also be due to the F peak rising in altitude; fewer available neutrals lead to less recombination occurring, and the signal strength will once again decrease.

Table 2.1: Rate coefficients for 630.0-nm emission. After Link & Cogger [14].

Coefficient	Rate	Units
A_{1_D}	$6.81\,\text{E-3}$	1/s
β_1	1.1	
k_1	$3.23\,\text{E-12}\ \exp(3.72/\tau_i - 1.87/\tau_i^2)$	cm^3/s
k_3	$2.0\,\text{E-11}\ \exp(111.8/T_n)$	cm^3/s
k_4	$2.9\,\text{E-11}\ \exp(67.5/T_n)$	cm^3/s
k_5	$1.6\,\text{E-12}\, T_e^{0.91}$	cm^3/s
T_i/T_e	Ion/Electron Temperature	K
τ_i	$T_i/300$	
T_n	Neutral Temperature	K

2.3 F-Region Dynamo

A main reason for studying the neutral winds is the dynamo process in the F region, through which the mechanical motion of the neutral particles creates an electrical forcing. The neutral wind, $\mathbf{U}$, is driven by a multitude of forces including pressure gradient force, gravity, Coriolis force, ion-neutral collisions, and the viscosity of air [15]:

$$d\mathbf{U}/dt = \mathbf{F} - \mathbf{g} - 2\Omega \times \mathbf{U} + KN(\mathbf{V} - \mathbf{U}) + (\mu/\rho)\nabla^2\mathbf{U}. \tag{2.6}$$

The pressure gradient force per unit mass is denoted by $\mathbf{F}$, gravity, $\mathbf{g}$, is a downward force term, Ω is the angular velocity of the earth, which is needed to describe the Coriolis effects, KN is the neutral-ion collision frequency, $\mathbf{V}$ is the ion drift velocity, μ is molecular viscosity, and ρ is the density. All vectors will be in an east-north-up (u, v, w) coordinate frame.

In general, the position of the sun drives the neutral wind's direction and speed. The pressure gradient force is the largest driving factor of meridional winds at the equator, causing an equatorward wind in the summer and a poleward wind in the winter. Zonally, the winds are eastward during the early night and shift to westward at dawn. These trends can be seen using the Horizontal Wind Model '93 (HWM93 [16]). The meridional and zonal winds at 250 km over northeastern Brazil have been modeled during 2011 using HWM93 with daily K_p indices as inputs. The K_p index is a standardized three-hour average of several different observatories' measurement of the horizontal component of the magnetic field used to quantify geomagnetic ac-

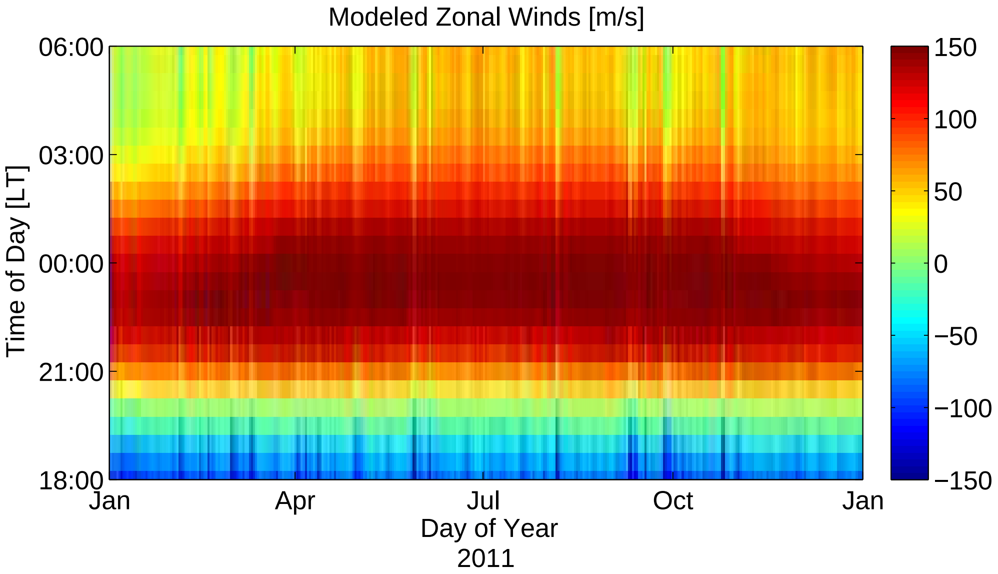

Figure 2.3: HWM93 predicted nighttime meridional wind over Brazil in 2011.

tivity [17]. The index quantifies the fluctuation of geomagnetic field with the integer values 0 to 9, where ∼1 is calm and greater than 5 is stormy. The meridional winds are displayed in Figure 2.3 and the zonal winds are displayed in Figure 2.4. Note the day-to-day fluctuations in velocity due to variance in magnetic field and solar flux.

The plasma velocity, **V**, or ion drift, is described by the following equation [15]:

$$\mathbf{V} = \mathbf{V_{E\times B}} + \mathbf{V_{U\cdot B}} + \mathbf{V_{diff}}. \tag{2.7}$$

The electromagnetic drifts are defined as

$$\mathbf{V_{E\times B}} = \frac{(\mathbf{E}\times\mathbf{B})}{B^2} \tag{2.8}$$

where **B** is the earth's magnetic field which points more or less horizontally northward at the magnetic equator and **E** is an electric field.

The neutral wind, **U**, also affects ions by pushing them along geomagnetic field lines. This velocity is a simple projection of the neutral wind onto the geomagnetic field line **B**:

$$\mathbf{V_{U\cdot B}} = \frac{(\mathbf{U}\cdot\mathbf{B})\mathbf{B}}{B^2}. \tag{2.9}$$

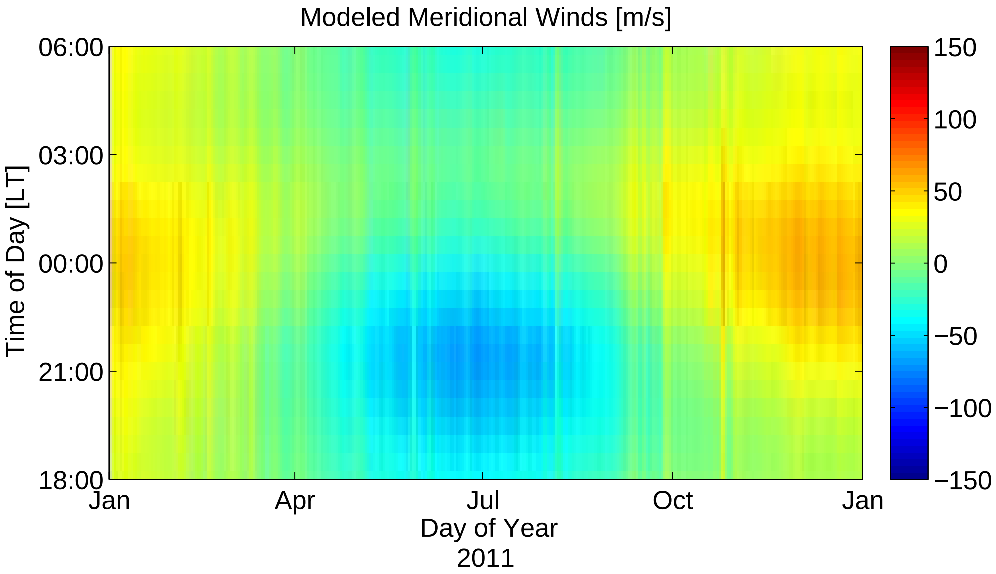

Figure 2.4: HWM93 predicted nighttime zonal wind over Brazil in 2011.

The final term, $\mathbf{V_{diff}}$, is the velocity due to plasma diffusion. This speed depends on the changes in plasma concentration, the changes in temperature, gravity, and the plasma diffusion coefficient [15].

In order to understand the dynamo process, the typical electric fields must first be understood. On the dayside of the earth, the sun's radiation heats and ionizes part of the upper atmosphere near the equator. The heating leads to expansion, causing a neutral wind and plasma drift both poleward and westward. The poleward plasma drift crossed with the magnetic field (it has a dip angle towards the poles) causes charge separation. Positive charge will accumulate at the dawn terminator and negative charge will accumulate on the dusk terminator due to Lorenz forcing:

$$\mathbf{F} = q(\mathbf{E} + \mathbf{V} \times \mathbf{B}). \tag{2.10}$$

Figure 2.5 is a northern hemisphere view of the planet that shows this charge build-up. The charge difference creates a dawn-to-dusk **E**, pointing to the east in daylight and pointing to the west during the night. The **E** fields that are set up then create drifts (Equation 2.7) due to the northern-pointing **B** field; the daytime eastern electric field produces an upward vertical drift, and the nighttime western electric field produces a downward vertical drift.

To further understand how the zonal neutral winds affect the drifts, it is

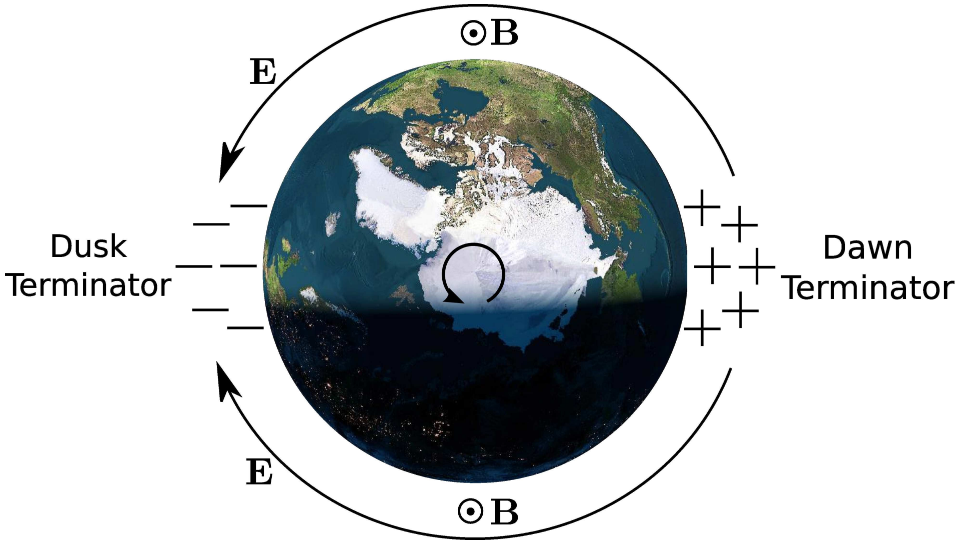

Figure 2.5: Charge accumulation and zonal **E** field around the earth. After Kelley [9].

first important to discuss the electrical current in a conducting slab, which Kelley [9] writes as

$$\mathbf{J} = \sigma(\mathbf{E} + \mathbf{U} \times \mathbf{B}). \tag{2.11}$$

The conductivity tensor, where **B** is parallel to the north in an east-north-up coordinate frame, is defined as

$$\sigma = \begin{pmatrix} \sigma_P & 0 & \sigma_H \\ 0 & \sigma_0 & 0 \\ -\sigma_H & 0 & \sigma_P \end{pmatrix} \tag{2.12}$$

where σ_P is the Pedersen conductivity, σ_H is the Hall conductivity, and σ_0 is the specific conductivity. A typical profile of these values at solar maximum is seen in Figure 2.6. The current is created from a wind through the particle-plasma interactions. There can be no divergence in current because the magnetic field lines terminate in an insulating region; this happens to be the E region which recombines during the night. A "slab" of conductivity remains in the F region when this lower altitude recombines. The neutral wind, blowing eastward at night due to the pressure gradient force, will create a vertical current (Equation 2.11). The current will move positive charge upward, but it will begin to accumulate on the edge of the conducting slab. The potential from charge separation forms a downward **E** field and current

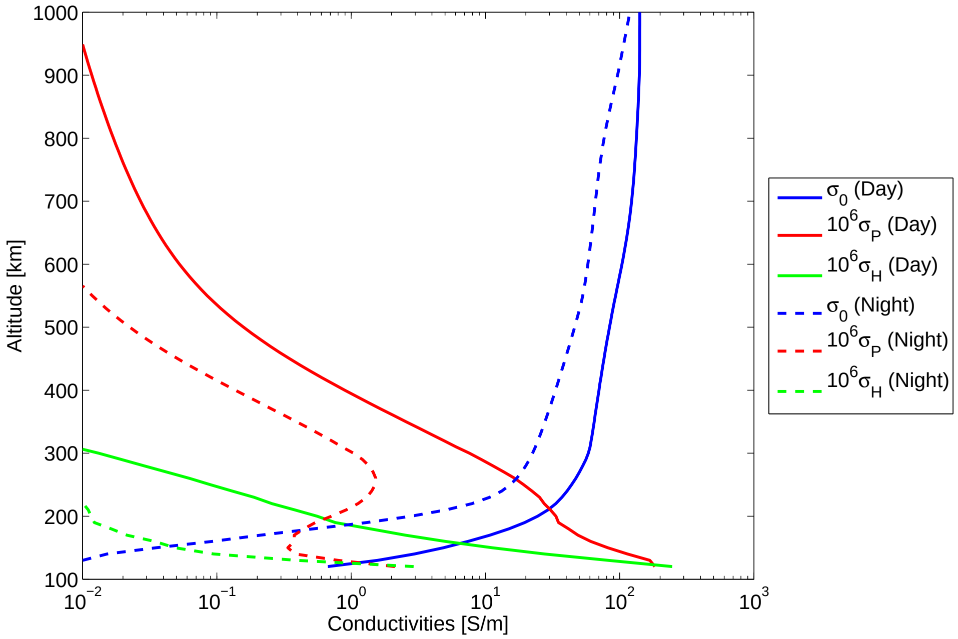

Figure 2.6: Typical profiles of ionospheric conductivities. After Kelley [9].

to negate the upward current and satisfy the divergence free condition. That **E** crossed with **B** leads to the typical eastern ion drifts during the night. This process, tying neutral winds into the plasma drifts, is termed the F-region dynamo.

2.3.1 Temperatures

The temperature of the thermosphere is typically around 1000 K due to the absorption of high energy photons (UV and EUV) from the sun. As the sun sets, the temperature starts to decrease through the night to roughly 750 K. The incoming radiation also changes across the year due to solar zenith angle, with higher temperatures in local summer. Similarly, the sun's 11-year solar cycle affects the temperatures cyclically; at 250 km the temperatures can range from around 600 K during deep solar minimum to 1200 K nearing solar max. There is also a midnight temperature maximum (MTM), a seasonally varying phenomenon in which tidal forcing causes a temperature bulge around local midnight [18].

A simulation of predicted thermospheric temperature conditions at 250

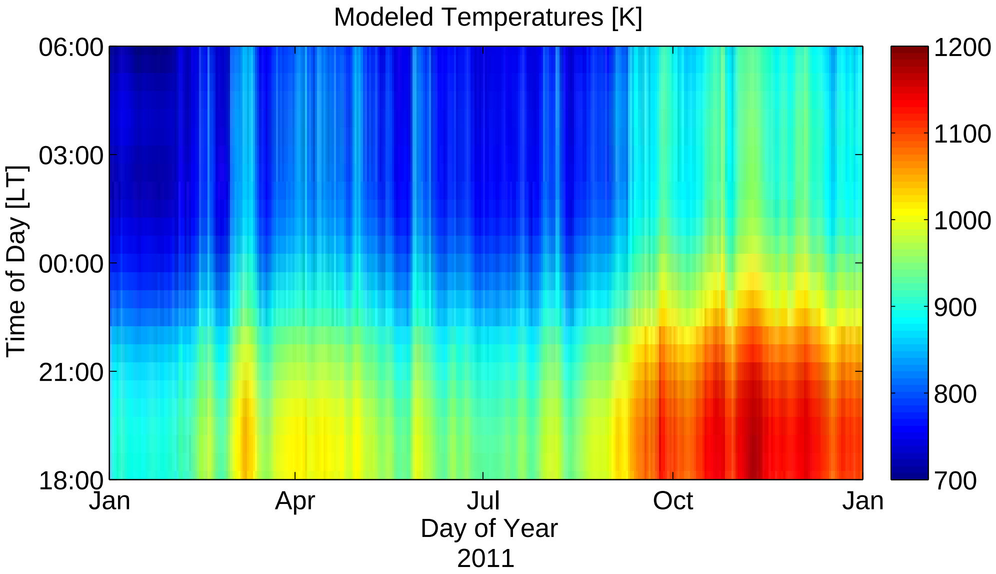

Figure 2.7: MSISE00 predicted nighttime neutral temperatures over Brazil in 2011.

km over northeastern Brazil (7.13°S, 37.54°W) from 2011 is shown in Figure 2.7. The data are modeled using the Naval Research Laboratory's Mass Spectrometer and Incoherent Scatter Empirical model (NRLMSISE-00) that takes the time of day, location, K_p index, and $f_{10.7}$ (a measure of solar flux at the 10.7-cm wavelength) as an input to show the day-to-day variation in temperature [5]. Note that while the general trend is a gentle falloff over the night, this model fails to capture the MTM that does indeed exist at this location [19].

2.3.2 FPI Measurements of Airglow

People have long observed the glowing ionosphere at night, mainly through auroral observations. The first Fabry-Perot interferometer observations of the aurora were made by Babcok [20] in 1923. Fifty years later, Hernandez and Roble became the first to record measurements of thermospheric winds and temperatures using the 630.0-nm emission [21]. In 1982, Biondi and Sipler were the first to collect airglow data from Brazil using an FPI [2]. Today, many more FPIs are scattered around the globe, but measurements of the neutrals, especially around the low latitudes and in the southern hemisphere, are lacking (see Figure 2.8).

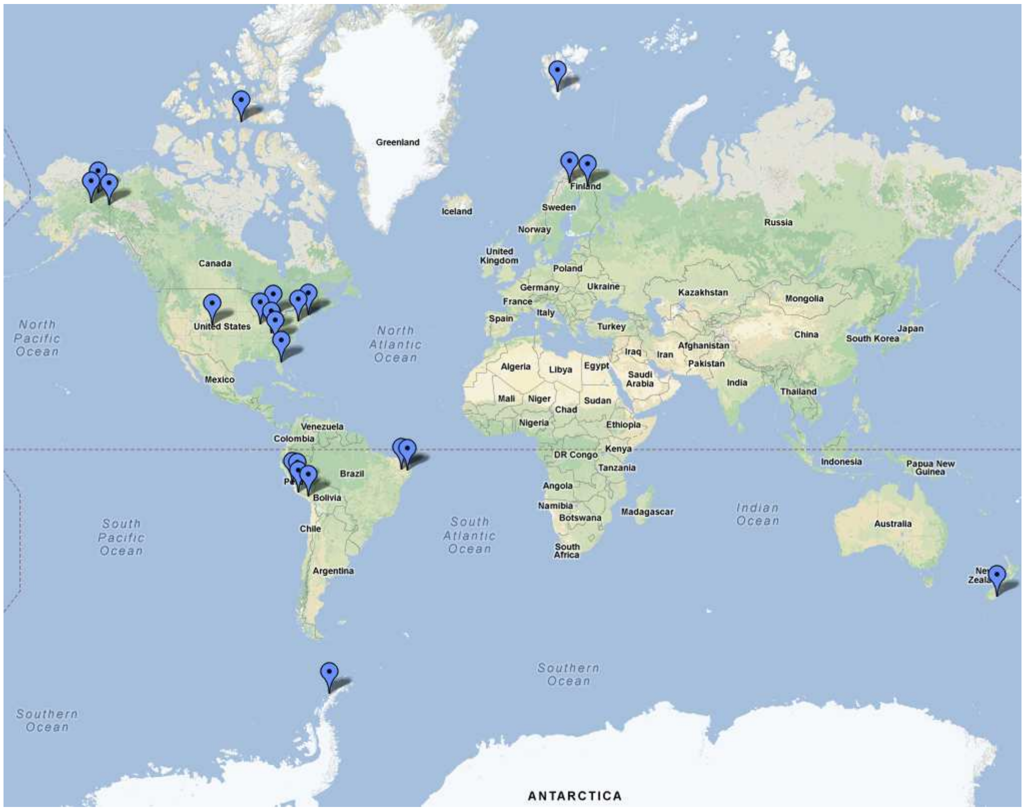

Figure 2.8: Map of known working FPI sites across the globe in 2012.

Observing vertical winds is a major focus of this thesis since knowing this component is necessary for analyzing the airglow observations. They were first estimated from the continuity equation and circulation models, and were computed to be on the order of 1 m/s [22]. Through the addition of more and more neutral wind data, it was found that the average vertical winds should be zero. However, Biondi and Sipler [2] were the first to show measurements of large downward vertical winds over Natal, Brazil. Later, Raghavarao [4] used the spectrometer on Dynamic Explorer 2 to propose that substantial vertical winds could be produced from the equatorial anomaly, especially around twilight hours when the downward winds were observed to be as high as 40 m/s. Additional measurements will be key in understanding the complex physics that occur in the *F* region. These neutral data will also help the atmospheric models, many of which are empirical (such as MSIS [5], HWM [6]). Other models are physics based (such as WAM [7] and TIE-GCM [23]) and will require this neutral data set as a means of validation.

CHAPTER 3

INSTRUMENTATION

In this chapter, the current setup of the RENOIR FPIs will be explained. A basic overview of the fundamental workings of an FPI as well as a description of the system's parameters are also included.

3.1 The Fabry-Perot Interferometer

Fabry-Perot interferometers (FPIs) are used in telecommunication products, lasers for resonance, interferometry, and spectroscopy. Ours is employed to measure the thermospheric temperatures and neutral winds of the F region by capturing the interference pattern of light after it passes through an etalon. The etalon is simply two partially-reflective pieces of flat glass separated by a gap. This optical cavity sets up a transmission function depending on the etalon's parameters and the wavelength of light inside the gap. The light that is transmitted interferes with itself creating the Airy interference pattern when imaged. The basic FPI system is composed of a filter, an etalon, a focusing lens, and a CCD.

3.1.1 Etalon Basics

The FPI's most important component is the etalon. It is made of two partially reflecting surfaces separated by a gap of distance d with a refractive index of n. These two surfaces are covered by a semi-reflective lossless coating giving the system a set reflectance, R, and transmittance, T.

To understand how temperature and wind estimates are made using an FPI, one must first understand the typical interference pattern created by the etalon. Begin by assuming that a monochromatic ray of light travels into the etalon at angle θ. This ray of light will be repeatedly transmitted and

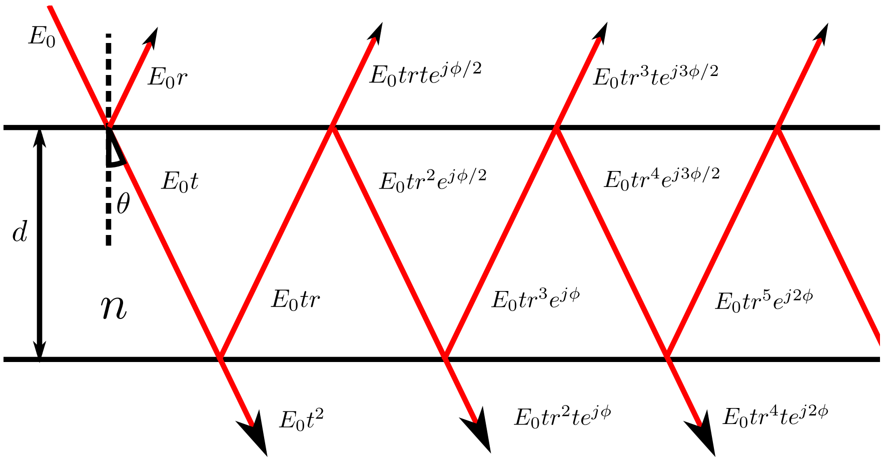

Figure 3.1: Etalon ray geometry.

reflected by the surfaces as seen in Figure 3.1. The optical path difference between successive reflections creates a phase lag, ϕ, shown to be [24]

$$\phi = \left(\frac{2\pi}{\lambda}\right)2dn\cos(\theta). \tag{3.1}$$

The total intensity of the transmitted electric field, E_T, can be calculated using simple geometric optics; by adding all the transmitted rays that emerge from the etalon,

$$\begin{aligned} E_T &= \sum E_{\text{transmitted}} \\ &= E_0t^2 + E_0tr^2te^{j\phi} + E_0tr^4te^{j2\phi} + ... \end{aligned} \tag{3.2}$$

Note that assuming both surfaces are identical, $R = r^2$ and $T = t^2$. Also, assume that the etalon is infinitely long so that an infinite geometric Taylor series can be used to simplify the summation [24]:

$$\begin{aligned} E_T &= E_0t^2(1 + r^2e^{j\phi} + r^4e^{j2\phi} + ...) \\ &= E_0t^2/(1 - r^2e^{j\phi}) \\ &= E_0T/(1 - Re^{j\phi}). \end{aligned} \tag{3.3}$$

The intensity of the light passing through is equivalent to $|E_T|^2$. Since we know $R + T = 1$, this intensity can be calculated and simplified with the use

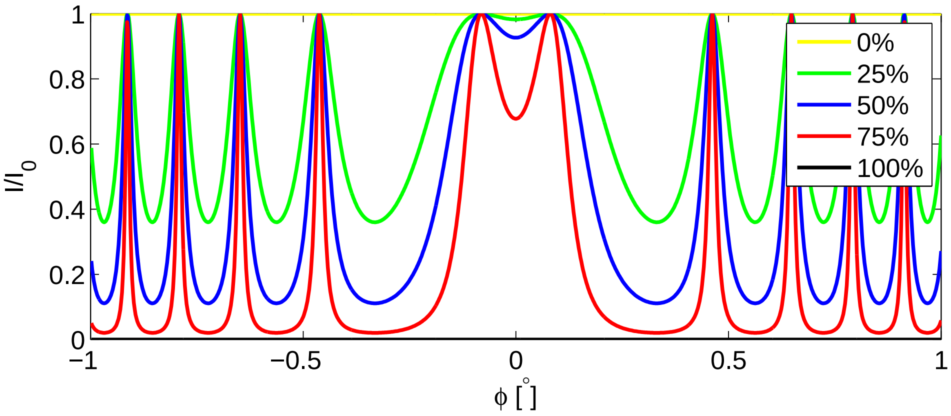

Figure 3.2: Sample Airy function with varied reflectance.

of a double angle identity:

$$\begin{aligned} I(\phi) &= I_0 T^2/(1 - Re^{j\phi} - Re^{-j\phi} + R^2) \\ &= I_0 T^2/(1 - 2R\cos(\phi) + R^2) \\ &= I_0 T^2/(1 - 2R(1 - \sin(\phi/2)) + R^2) \\ &= I_0 T^2/((1 - R)^2 + 4R\sin^2(\phi/2)) \\ &= I_0 T^2/(1 - R)^2(1 + F\sin^2(\phi/2)) \\ &= I_0/(1 + F\sin^2(\phi/2)). \end{aligned} \tag{3.4}$$

We see that the intensity is equal to the Airy function, where $F = 4R/(1-R)^2$ is the coefficient of finesse. Figure 3.2 shows about five full fringe orders of this function with various reflectance values. The Airy function is a two-dimensional pattern, and since the CCD used is a 2D array, we see a radially symmetric pattern as in Figure 3.3. If measured with a 1D CCD array, only the 1D fringe pattern is seen.

3.1.2 Etalon Parameters

There are several parameters in an FPI design that can be chosen to optimize the output for a specific application. Figure 3.2 clearly demonstrates that fringes can be narrowed just by selecting a higher reflectance coating. The airglow temperature estimation is derived from the fringe thickness; thinner fringes means less overlap and better accuracy. There is a balance to achieve, however, as increasing the reflectance decreases the transmitted sig-

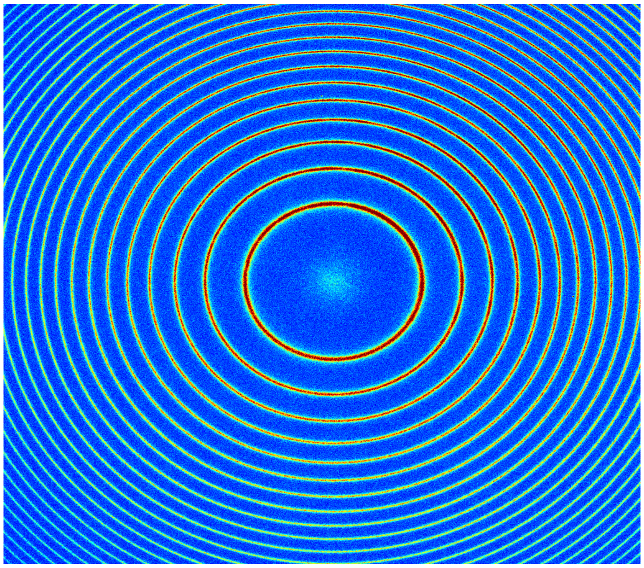

Figure 3.3: Typical CCD image of rings formed when light from a HeNe laser is imaged through the etalon.

nal and thus lowers the SNR. Reflectivity finesse, N_R, is a useful parameter to characterize peak spacing versus width. The transmission peaks are located at every $\phi = 2n\pi$ interval, where n is the fringe order. The full-width at half-max (FWHM) will occur at phase lag ϕ_{FWHM} in Equation 3.4 such that

$$1/2 = 1/(1 + F\sin^2(\phi_{FWHM}/2)). \tag{3.5}$$

The reflectivity finesse is then simply defined as the ratio between the separation and width [24]:

$$N_R = 2\pi/2\phi_{FWHM} = (\pi/2)\sqrt{F}. \tag{3.6}$$

Another very important parameter is the free spectral range (FSR or $\Delta\lambda$) that describes the maximum change in wavelength that can be unambiguously resolved by the system. It categorizes the resolving power of the system. By taking the derivative of Equation 3.1 with respect to wavelength, we can find how the phase shift changes with wavelength shift from a fixed input angle:

$$\Delta\phi = 2\pi 2dn\cos(\theta)\Delta\lambda/\lambda^2. \tag{3.7}$$

The smallest possible phase change, $\Delta\phi$, that would cause the new fringes to overlap the old fringes and be undetectable would be 2π. Setting Equation 3.7 equal to this phase change, we find the FSR:

$$\Delta\lambda = \lambda^2/(2dn\cos(\theta)). \tag{3.8}$$

Note that since our frequency is fixed by the airglow, d and n are the free parameters that adjust the FSR. The free spectral range is proportional to the largest unambiguous Doppler shift of airglow winds. While having a higher free spectral range gets better frequency resolution, the optical field-of-view (FOV) is set and thus less fringes will be imaged.

A final parameter that is useful is the resolution power of the etalon, R_0. This is used to determine the resolving limit between two partially overlapping peaks. The Rayleigh criterion for resolution states that peaks can be separated if the ratio of the midpoint intensity and peak intensity is $8/\pi^2$ [24]. The resolution power is defined as

$$R_0 = \Delta\lambda/N_R. \tag{3.9}$$

3.1.3 Parameters with Real Signals

While the previous parameters are useful in understanding an FPI system, they all assume an idealized delta-Dirac function input. In reality, the input is a Gaussian broadened source centered at the peak wavelength we seek to measure. The airglow intensity per pixel, i, can be estimated from

$$N_i = \frac{10^6\, A_0 \Omega_i t Q_i T_E}{4\pi} \int T_F(\lambda)\Upsilon(\lambda,\theta)S(\lambda)\,\mathrm{d}\lambda + B_i \tag{3.10}$$

where A_0 is the area of the etalon, Ω_i is the field-of-view, t is the integration time, Q_i is the efficiency of the CCD pixel, T_E is the transmission coefficient of the etalon, T_F is the transmission coefficient of the filter, Υ is the instrument function, S is the Gaussian spectrum of the input signal, and B_i is the background noise of the current pixel. This shows that the actual output of an FPI is the convolution of the signal (a Gaussian) with the etalon instrument function (the Airy function). The result is a broadened Airy pattern shifted by the Doppler frequency which contains the signal parameters we desire to

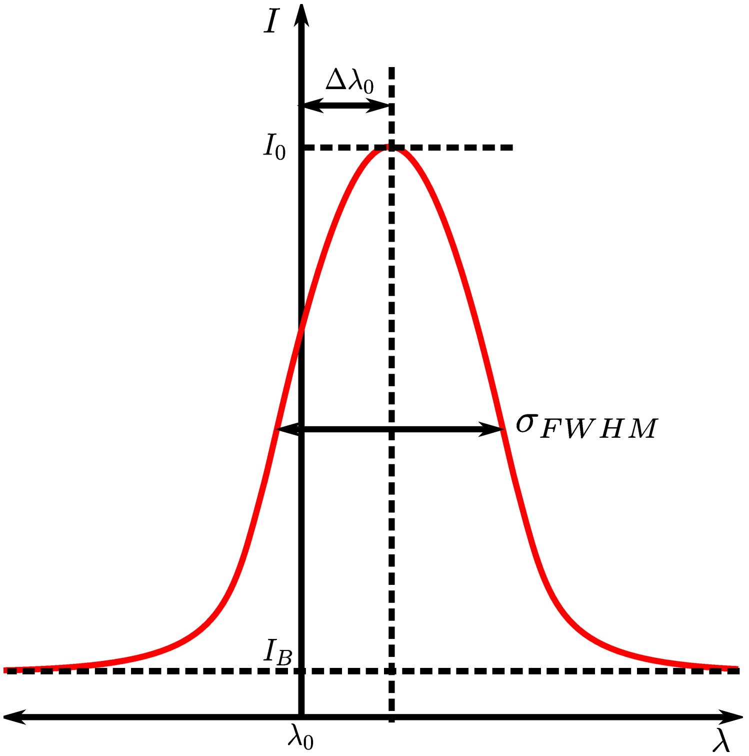

Figure 3.4: Signal parameters desired from the measurements of a single fringe.

measure.

Figure 3.4 shows the four main signal parameters that will be retrieved from a single fringe: background intensity, peak intensity, Doppler broadening, and Doppler shift. The background intensity, I_B, gives a measure of the noise level in the image. The airglow intensity, I_A, is measured from the difference between I_0 and I_B and can be used to estimate k_{6300} (see Equation 2.5). The neutral temperature, T_n, is calculated from the Doppler broadened width, σ_{FWHM}. This FWHM is proportional to $\sqrt{2kT_n/m}$, where k is Boltzmann's constant and m is the mass of the constituent (oxygen) [25]. The line-of-sight winds, V^{LOS}, can be determined by using the Doppler shift, $\Delta\lambda_0$. The standard Doppler shift equation is given as

$$f = \left(\frac{c + V^{\mathrm{r}}}{c + V^{\mathrm{s}}}\right) f_0. \tag{3.11}$$

As a stationary observer of the airglow, $V^{\mathrm{r}} = 0$ and the Doppler equation is solvable for the source velocity, $V^{\mathrm{s}} = V^{\mathrm{LOS}}$:

$$\begin{aligned} V^{\mathrm{LOS}} &= \left(\frac{\Delta f_0}{\Delta f_0 + f_0}\right) c \\ &= \left(\frac{\Delta\lambda_0}{\lambda_0}\right) c. \end{aligned} \tag{3.12}$$

This equation may seem straight forward, but the problem lies in knowing the peak location of λ_0. Obtaining a proper zero-Doppler reference is crucial in getting a correct Doppler shift and accurate winds. Such techniques will be discussed further in Chapter 4.

3.2 Fabry-Perot Sites

In 2009, two RENOIR (Remote Equatorial Nighttime Observatory for Ionospheric Regions) systems were deployed in northeastern Brazil to monitor the thermosphere near the equator. One is stationed in the city of Cajazeiras (6.87°S, 38.56°W, geomagnetic: 5.73°S, 32.98°E) and the other at Cariri (7.38°S, 36.52°W, geomagnetic: 6.81°S, 34.70°E). The instrumentation in these systems includes an airglow imager, a dual frequency GPS unit, GPS scintillation monitors, and Fabry-Perot interferometers. While the GPS units can run continuously throughout the day and night measuring total electron content (TEC: receiver to satellite integrated electron density), the imaging systems can only view the redline emission after sunset during moon-down time periods (the bright moon is a large noise source).

3.2.1 RENOIR FPI Parameters

The FPIs in Brazil use a 4.2-cm diameter glass etalon with a 1.5-cm air gap spacing ($n = 1.0006$) to image the 630.0-nm redline emission. They each have a 76% reflectivity while the filter has approximately a 65% 630.0-nm transmission efficiency with a full-width half-max of approximately 0.6 nm. The image is focused onto a 13.3x13.3 mm (1024x1024 pixel) CCD by a lens with a focal length of 30 cm. The CCD purchased is an Andor DU434 which has an extremely low readout noise of 3 electrons/pixel and a dark noise of 0.0004 electrons/pixel when cooled to below -70 °C. The line-of-

Figure 3.5: SkyScanner looking south in Cariri.

Table 3.1: Parameters concerning FPI.

Parameter	Variable	Value
Etalon Diameter	D	4.2 cm
Etalon Gap	d	1.5 cm
Refractive Index	n	1.0006
Etalon Reflectivity	R	76%
Filter Transmission	T	65%
Filter FWHM		0.6 nm
CCD Dimensions		1024x1024 pixels
CCD Pixel Size		13x13 μm
CCD Readout Noise		3 e^{-}/pixel
CCD Dark Noise		0.0004 e^{-}/pixel
SkyScanner FOV	θ	1.8°

sight wind direction is set using a two-axis pointing mirror system called a SkyScanner (see Figure 3.5). Two motors control the azimuthal and zenith tilt of the mirrors within 0.1°, allowing for full sky coverage from the 1.8° half-angle field of view. The etalons, lenses, and filters are all encased in a temperature controlled box to minimize the change in the parameters due to the diurnal temperature cycle. A Melles Griot STP 910-230 HeNe laser is used for measuring the instrument function. It is stated to lock within 10 minutes between 10 and 30 °C and to be stable within 3 MHz over 8 hours. There is also a maximum of a 0.5-MHz/°C drift in an unstable environment. The laser image is taken by observing a diffusion sphere with the 632.8-nm HeNe source shining into it.

Using Equation 3.8 along with our system parameters in Table 3.1, we find the FSR to be 13.23 pm. If this is applied to Equation 3.12, the maximum unambiguous Doppler shift can be calculated to be 6,295.6 m/s. The largest realistic line-of-sight wind speed in the ionosphere will be less than 300 m/s; this is well within the limits set by the FSR, meaning the etalon was properly designed to measure the desired winds. The field-of-view, θ_{FOV}, on the CCD is given by simple trigonometry:

$$\theta_{\mathrm{FOV}} = \tan^{-1}(l_{\mathrm{CCD}}/2f) \tag{3.13}$$

where f is the focal length and l_{CCD} is the width of the CCD. This equation, in conjunction with Equation 3.1, can be used to find the total phase from the center to the edge of the CCD. Simply divide this by 2π to get the estimated number of fully imagable rings:

$$N_{\mathrm{rings}} = (\phi|_{\theta=\theta_{\mathrm{FOV}}} - \phi|_{\theta=0})/2\pi. \tag{3.14}$$

Using the system parameters defined in Table 3.1, there should be 11.7 total rings.

3.2.2 Viewing Geometries

Initially, the FPIs were set up to look in the cardinal directions at a 45° elevation angle, as well as to zenith and to a calibration laser (the utility of which will be discussed in Chapter 4), to estimate the wind velocities and temperature in these directions. By assuming zero vertical wind throughout the night, geographically meaningful winds could be calculated from each image. The observation directions for the cardinal viewing mode are seen in Figure 3.6, where the tips of the arrows represent the latitude/longitude of the 250-km height from which the majority of the signal is assumed to come. Although the distances between different observations are large (>300 km), we assume the winds and temperatures are constant across this area. This assumption allows for comparisons to be made with the different viewing points and is reasonable in calm conditions (times with little fluctuation in the earth's magnetic field).

In the middle of 2010, the instruments were set up to run in a common

Table 3.2: Parameters concerning common volume geometry. After Meriwether [19].

	From CAJ	From CAR
Elevation Angle to CVN	55.6°	55.6°
Azimuth Angle to CVN	59.1°	329.1°
Distance to CVN	164.25 km	164.25 km
Elevation Angle to IN	64.2°	64.2°
Azimuth Angle to IN	104.1°	284.1°
Distance to IN	116.14 km	116.14 km
Elevation Angle to CVS	55.6°	55.6°
Azimuth Angle to CVS	149.1°	239.1°
Distance to CVS	164.25 km	164.25 km

volume (CV) mode. This synchronized sequence consists of a laser and zenith measurement followed by one or two common volume points and the inline point. The midpoint (inline) is located at 7.13°S, 37.54°W (geomagnetic: 6.28°S, 33.84°E). The north common volume point (denoted CVN) is located at 6.11°S, 37.29°W (geomagnetic: 5.26°S, 34.45°E) while the south common volume point (denoted CVS) is located at 8.14°S, 37.80°W (geomagnetic: 6.95°S, 33.22°E). The locations of these common volume points and the FPI locations are shown in Figure 3.7, where the arrow tip indicates the point where the observation pierces 250 km in altitude. These three points are seen from Cariri and Cajazeiras at the angles displayed in Table 3.2. CVN and CVS are chosen so that the horizontal wind components at 250 km are orthogonal and the elevation angles from each site are equal. This conveniently allows us, when a vertical wind assumption at these locations is made, to get a complete horizontal wind vector. Additionally, the inline measurement from two sites adds another vertical wind estimation.

3.2.3 Data Collection

The two RENOIR systems operate every night through a set of automated scripts. Their tasks range from turning on the equipment, to setting up the proper start/stop times for data recording, to actually starting the program that takes the measurements all night. The instruments begin taking data after astronomical twilight and run until dawn. The system is pre-programmed to be in either the cardinal or common volume viewing mode, and will take

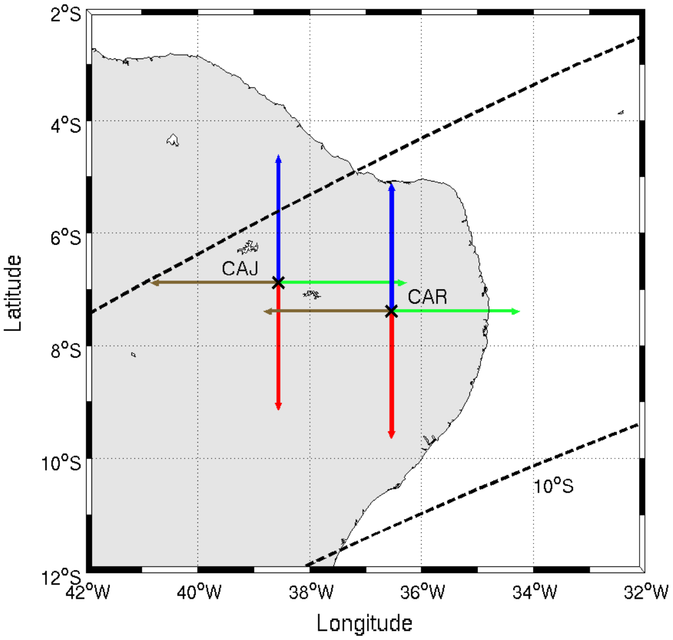

Figure 3.6: FPI measurement directions in cardinal mode: Arrows project to 250 km for the north (blue), east (green), south (red), and west (brown) directions. The 10° geomagnetic latitude line is drawn in dashed black for reference.

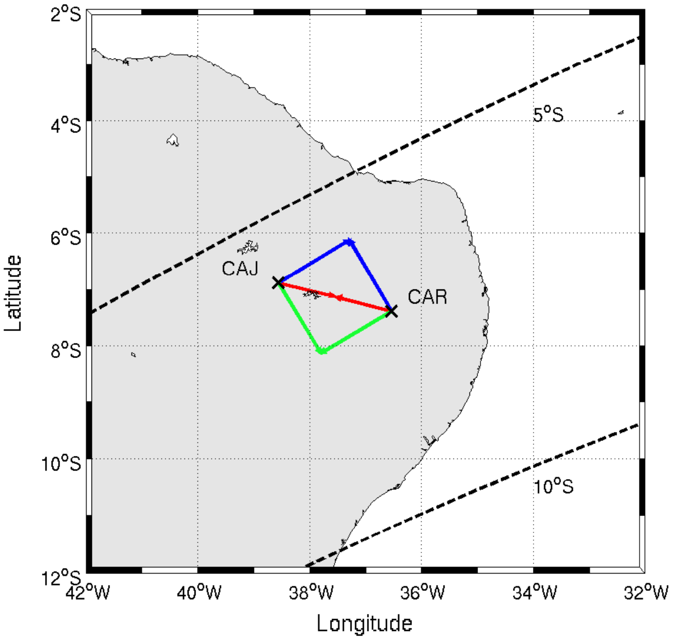

Figure 3.7: FPI measurement directions in common volume mode: Arrows project to 250 km height for the north (blue), inline (green), and south (green) directions. The 10° geomagnetic latitude line is drawn in dashed black for reference.

a designated sequence of images the entire night. Laser exposures are a mere 30 seconds, while airglow exposures range from 3 to 5 minutes, depending on solar conditions. Once the night is over, all laser, zenith, and directional images are sent back to a University of Illinois server for processing.

CHAPTER 4

FPI DATA ANALYSIS AND ZERO-DOPPLER TECHNIQUES

This chapter discusses the analysis techniques used to convert an interferogram from the FPI into the scientifically desired values of intensity, temperature, and Doppler velocity. The exact analysis relating to the equations in Section 3.1.3 will be covered, along with a comparison of zero-Doppler techniques. A 630.0-nm calibration source is not easily obtainable, so one of three zero-reference methods must be substituted to overcome this challenge.

4.1 FPI Analysis Overview

With an entire night's worth of interferograms collected, custom MATLAB programs automatically run to analyze the observations. The goal of the processes is to transform each two-dimensional (2D) image into a one-dimensional (1D) fringe pattern from which winds and temperatures can easily be extracted. The processing can be broken down into three stages: laser exposure images, sky exposure images, and grouped measurement correction. A brief overview of these scripts follows; for a more detailed explanation, see Makela et al. [25].

The laser images are analyzed first to determine the instrument function throughout the night; the HeNe laser has such a narrow bandwidth that the interferogram created from the laser exposure will approximate the impulse response of the system. This method of finding the instrument function was adapted from Killeen and Hays [26]. Although the laser exposures are shorter than the sky exposures, the HeNe emission is much brighter, and this results in a high SNR, creating easily analyzable rings. First, the center of the interference pattern must be found through thresholding the image and placing bounding concentric circles on all the rings in the 2D Airy pattern. The center is recorded as the average of the centers of the bounding circles.

Due to the circular nature of the Airy pattern, an annular summation about the center is taken; hence, an accurate sub-pixel center is desired. Obtaining an accurate center is a challenging task to automate, and a poorly chosen center will induce large errors because the peak locations are smeared out and the Gaussian shape is artificially broadened.

Next, the 2D pattern is collapsed azimuthally around the center to a simpler 1D fringe pattern. An annular summation achieves this simplification using N bins that take the form of equal area rings to create a fringe pattern as seen in Figure 4.1. For full, 1024×1024 pixel images, we found that $N = 500$ is a good choice, and for half-resolution images, $N = 250$. A low N will have higher SNR per bin since each will have more pixels in it. However, there will also be poorer resolution of the fringes, making the parameter estimation harder. Empirical testing showed that the stated values of N annular regions were optimal at reducing the errors in parameter estimation while keeping the SNR high. Then, the peaks in the fringe pattern are found in pixel space. Each individual Gaussian-like order (centered on the each peak location) will be decomposed into 22 Fourier coefficients. These Fourier components are interpolated across the night in order to be used as the instrument function parameters in the airglow image analysis.

Next, the 630.0-nm airglow images are analyzed in a manner identical to the laser interferograms. The laser center point, peak locations, and Fourier coefficients are all used as initial guesses for better accuracy because the SNR for the laser is greater than for the airglow emissions. The frequency change between the two is corrected using K, a measure of peak-to-peak distance:

$$K = \frac{\lambda_0}{\lambda_{\text{laser}}} K_{\text{laser}}. \tag{4.1}$$

Once the Fourier coefficients are computed, they are used in the Levenberg–Marquardt (LM) non-linear least-squares fitting algorithm to compute estimates of the parameters describing the best-fit Gaussian to the order. This Gaussian is the signal, $S(\lambda)$, from Equation 3.10. The estimated parameters not only define the shape of the curve but also are used to deduce the background and signal intensity, Doppler velocity, and temperature. The LOS Doppler shift estimates the neutral wind speed using an arbitrary reference

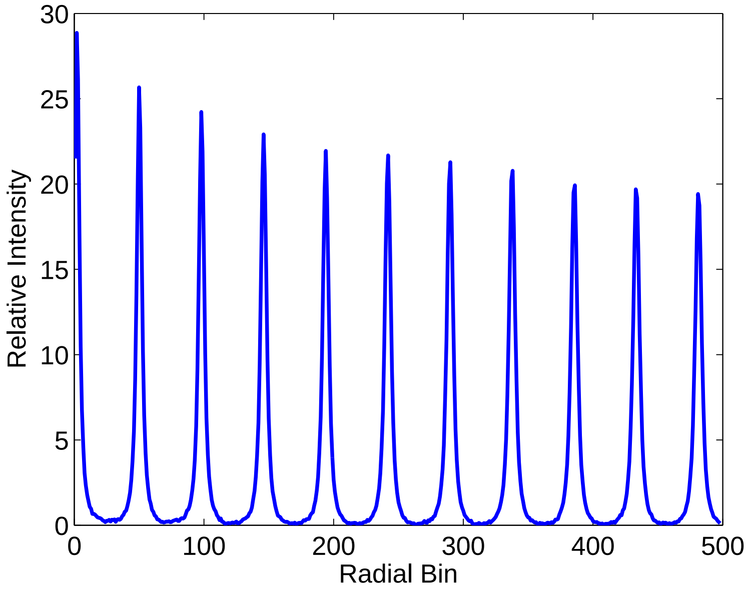

Figure 4.1: Typical 1D fringe pattern.

wavelength, λ_{ref}, and the LM peak position estimate, $\hat{\lambda}$:

$$V^{\mathrm{LOS}} = c\left(1 - \frac{\hat{\lambda}\Delta\lambda + \lambda_{\mathrm{ref}}}{\lambda_0}\right). \tag{4.2}$$

The neutral temperature is found using the molecular mass of oxygen, m, Boltzman's constant, k, and the LM estimate of width, $\hat{\sigma}$:

$$T = \frac{m}{2k}\left(\frac{\hat{\sigma}\Delta\lambda c}{\pi\lambda_0}\right)^2. \tag{4.3}$$

Finally, the entire night of laser and sky exposure Doppler velocity estimates is used to obtain corrected, geographically meaningful wind estimates. This step requires various assumptions to correct for not having an absolute zero-Doppler reference (see Section 4.2). After the LOS velocities are corrected, they are transformed into useful geographic winds (meridional, zonal, and vertical) and plots of the data are generated.

Before we can cover the Doppler analysis, a justification of the necessity of a zero-Doppler reference is required. The wavelength of the incoming light from the redline emission is unknown and the absolute phase cannot be measured from the interferogram. Without either of these, an absolute Doppler shift cannot be found. Thus, a zero-Doppler reference is needed

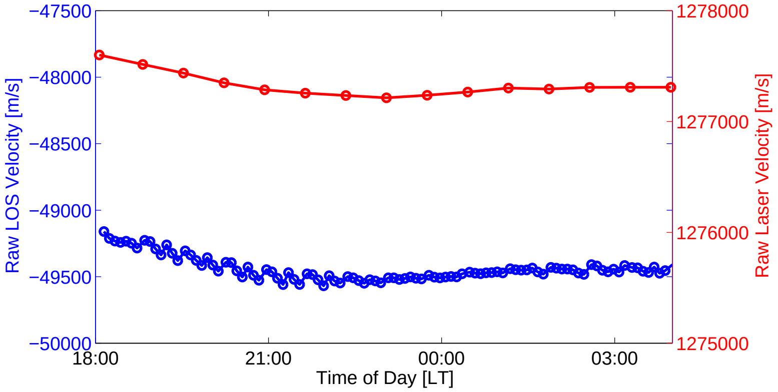

Figure 4.2: An entire night's uncorrected laser and raw LOS airglow velocities taken from LM's analysis of the second fringe on November 7-8, 2010 at Cariri.

so that accurate absolute velocity measurements can be made. Figure 4.2 shows a single night's uncorrected laser and line-of-sight Doppler velocities from the LM analysis. Note how the results are completely unreasonable; the maximum LOS wind speeds from thermospheric models are at most ±300 m/s, and, thus, some Doppler reference must be used to correct the offset. The next section discusses the possible choices for the zero offset.

4.2 Doppler Analysis

Each FPI measurement provides an estimate of LOS Doppler shift, which must be transformed into a sensible coordinate system, such as geographic east, north, and up. This Doppler shift can be calculated as a sum of projections of the u, v, w (east-north-up) winds onto the observation direction measured by the instrument. For instance, the vertical wind component of the LOS wind is calculated as $V_i^{\text{zenith}} = w\sin(\alpha_i)$ where α_i is the elevation angle. Figures 4.3 and 4.4 show the geometry of these projections and, thus, the total Doppler velocity is defined as:

$$V_i^{\text{LOS}} = w\sin(\alpha_i) + [v\cos(\theta_i) + u\sin(\theta_i)]\cos(\alpha_i) + \beta_i \tag{4.4}$$

where V is the observed velocity, β is the velocity offset due to unknown Doppler reference, and θ is the azimuthal angle. Superscripts will denote the

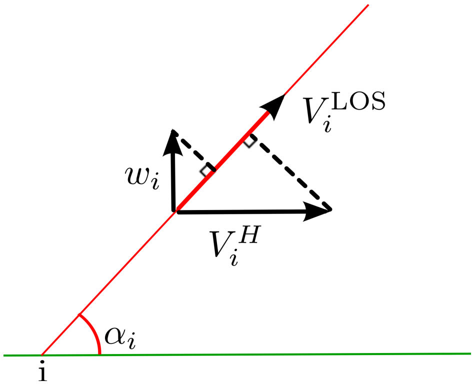

Figure 4.3: Velocity projection geometry of single FPI: elevation cut.

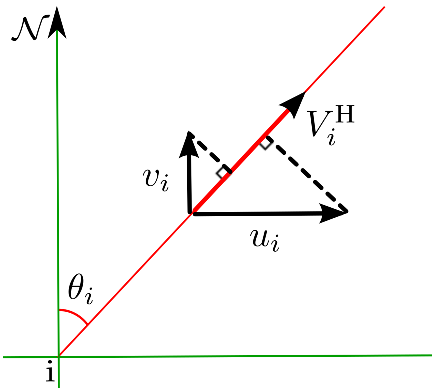

Figure 4.4: Velocity projection geometry of single FPI: azimuthal cut.

direction frame in which the wind measurement is given (e.g., LOS, zenith, or horizontal) and subscript i will denote the site where the measurement is made. β_i is the unknown Doppler reference described in Section 4.1. In one LOS measurement, there are four unknowns to solve for. The separate zenith and inline measurements eliminate the horizontal components, leaving only two unknowns to solve. However, these equations are still under-determined. In our bi-static RENOIR experiment, there are two measurements but still four unknowns, also making this an under-determined system. We have created three techniques to make this system of measurements solvable. The following techniques use "hat" notation to signify values estimated from observations and "tilde" notation to signify values interpolated across time.

4.2.1 Zero-Zenith Technique

A very straightforward method for determining the zero reference is to assume that the vertical winds are zero. Vertical winds are on the order of one to two magnitudes smaller than the horizontal winds (horizontal winds are typically 50 to 200 m/s). Due to the accuracy limitation of older equipment, although a slight vertical velocity was measured, the value of 0 m/s was usually contained within the error bars. Since uncertainty was so high in these measurements, it was safe to assume that the vertical winds during the night were actually zero. This assumption allows us to take the zenith measurements throughout the night and use these as a 630.0-nm Doppler

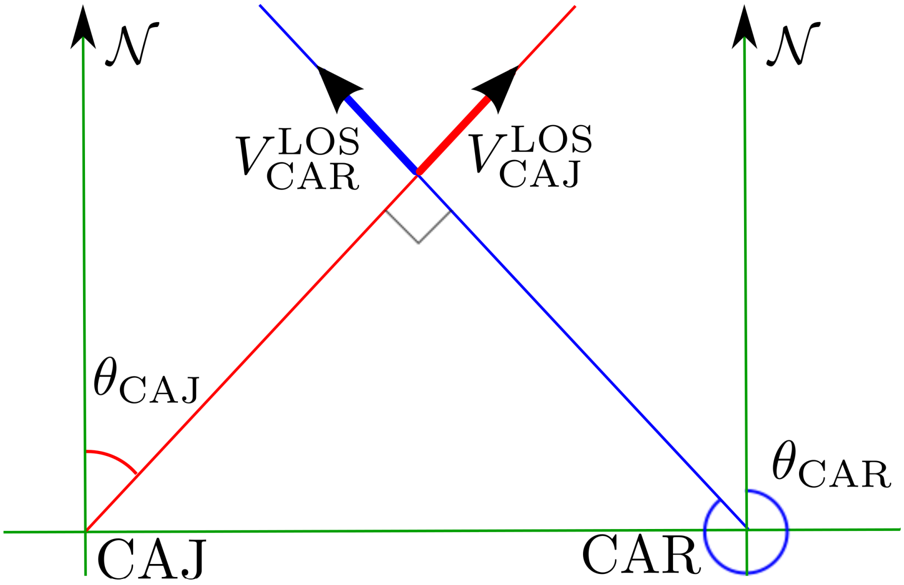

Figure 4.5: Aerial view of common volume viewing geometry.

zero reference. With this assumption, $\hat{w}$ is always set to be zero and we can use the zenith LOS measurements to solve for $\hat{\beta}_i(t)$. Doing so shows that $\hat{\beta}_i(t) = V_i^{\text{zenith}}(t)$, which is spline interpolated across the entire night for each site. This zero-Doppler reference simplifies Equation 4.4 for all non-zenith directions to

$$V_i^{\text{LOS}} = [v\cos(\theta_i) + u\sin(\theta_i)]\cos(\alpha_i) + \tilde{V}_i^{\text{zenith}} \tag{4.5}$$

where $\tilde{V}_i^{\text{zenith}}$ is the Doppler offset interpolated to this measurement time.

From this equation it is easily seen that when cardinal mode is active, the equation reduces to $V_i^{\text{cardinal}} = \hat{x}\cos(\alpha_i) + \tilde{V}_i^{\text{zenith}}$, where $\hat{x}$ is the estimated horizontal wind speed in the cardinal direction that the measurement is pointed in (i.e., north, south, east, or west). Thus, with one measurement, one component of the horizontal wind field can be solved:

$$\hat{x} = (V_i^{\text{cardinal}} - \tilde{V}_i^{\text{zenith}})/\cos(\alpha_i). \tag{4.6}$$

When in CV mode, the systems take horizontally perpendicular measurements at the common volume point, as shown in Figure 4.5. Once corrected for offset, the system of equations is just a rotation matrix, set up as

$$\begin{bmatrix} V_{\text{CAJ}}^{\text{LOS}} - \tilde{V}_{\text{CAJ}}^{\text{zenith}} \\ V_{\text{CAR}}^{\text{LOS}} - \tilde{V}_{\text{CAR}}^{\text{zenith}} \end{bmatrix} = \begin{bmatrix} \sin(\theta_{\text{CAJ}})\cos(\alpha_{\text{CAJ}}) & \cos(\theta_{\text{CAJ}})\cos(\alpha_{\text{CAJ}}) \\ \sin(\theta_{\text{CAR}})\cos(\alpha_{\text{CAR}}) & \cos(\theta_{\text{CAR}})\cos(\alpha_{\text{CAR}}) \end{bmatrix} \begin{bmatrix} \hat{u} \\ \hat{v} \end{bmatrix}. \tag{4.7}$$

The vector wind components at the common volume location are then solved to be

$$\hat{u} = \frac{V_{\text{CAJ}}^{\text{H}}\cos(\theta_{\text{CAR}}) - V_{\text{CAR}}^{\text{H}}\cos(\theta_{\text{CAJ}})}{\sin(\theta_{\text{CAJ}} - \theta_{\text{CAR}})} \tag{4.8}$$

$$\hat{v} = \frac{V_{\text{CAJ}}^{\text{H}}\sin(\theta_{\text{CAR}}) - V_{\text{CAR}}^{\text{H}}\sin(\theta_{\text{CAJ}})}{\sin(\theta_{\text{CAR}} - \theta_{\text{CAJ}})} \tag{4.9}$$

$$\hat{w} = 0 \tag{4.10}$$

where the horizontal components are

$$V_{\text{CAJ}}^{\text{H}} = \frac{V_{\text{CAJ}}^{\text{LOS}} - \tilde{V}_{\text{CAJ}}^{\text{zenith}}}{\cos(\alpha_{\text{CAJ}})} \tag{4.11}$$

$$V_{\text{CAR}}^{\text{H}} = \frac{V_{\text{CAR}}^{\text{LOS}} - \tilde{V}_{\text{CAR}}^{\text{zenith}}}{\cos(\alpha_{\text{CAR}})}. \tag{4.12}$$

Using these equations, the Brazilian data were analyzed for neutral wind speeds. A single example of this analysis on a night of clear-sky common volume measurements is shown in Figure 4.6. These results are reasonable and agree with results from both cardinal mode and climatological models. However, the next-generation FPIs currently in use are more accurate and have smaller measurement uncertainties and, therefore, should be able to measure vertical winds (that were initially assumed to be zero). We can test the accuracy of this assumption using the independent inline measurement of vertical wind. The vector addition of the corrected inline directions (geometry in Figure 4.7) only has a vertical component because the horizontal components should be nearly equal and opposite. The remaining vertical component is an estimation of the vertical wind:

$$\hat{w}^{\text{IN}} = \frac{V_{\text{CAJ}}^{\text{IN}} - \tilde{V}_{\text{CAJ}}^{\text{zenith}} + V_{\text{CAR}}^{\text{IN}} - \tilde{V}_{\text{CAR}}^{\text{zenith}}}{2\sin(\alpha^{\text{IN}})}. \tag{4.13}$$

When comparing the vertical winds from the bottom plot of Figure 4.6, the inline vertical measurements are not self-consistent with the zenith estimated

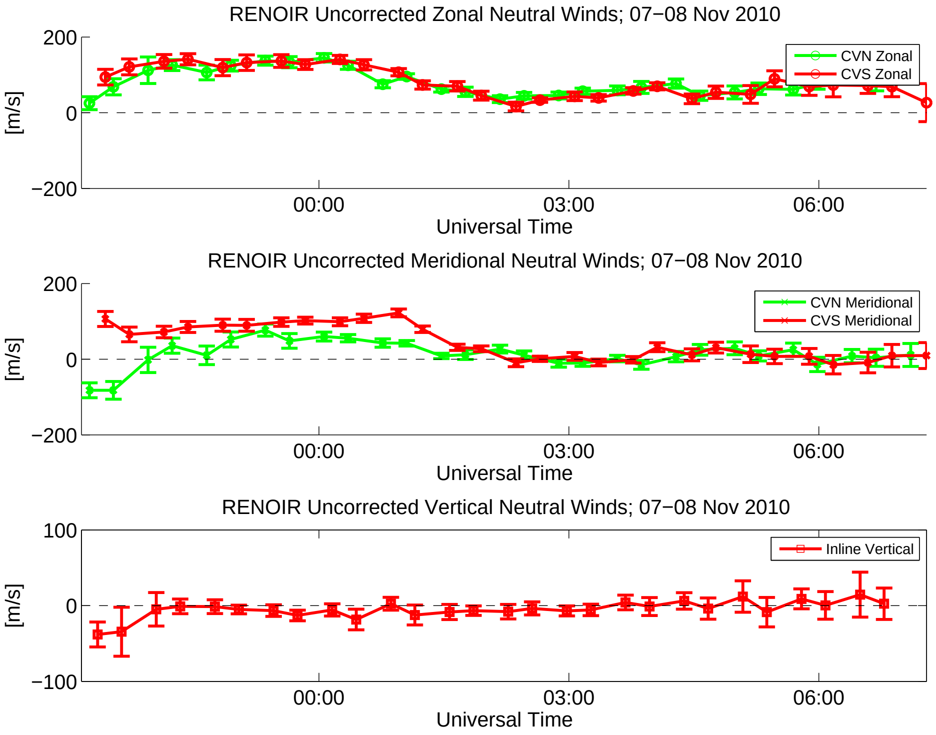

Figure 4.6: Common volume winds analyzed using zero-zenith technique on November 7-8, 2010.

vertical winds (which were assumed to be zero) at each site, implying that our assumptions are wrong. This is not an isolated instance; many nights, particularly in the local summer, have a nearly −40 m/s vertical wind at dusk. These observations match similar findings by Raghavarao [4] and has thus prompted a new method of Doppler zeroing to be created.

4.2.2 Zero-Laser Technique

In order to not have to assume zero vertical wind in the thermosphere, a priori, an alternate method for determining the Doppler zero reference is needed. A frequency-stabilized HeNe laser is already in use for deriving system parameters for the analysis, so the stationary laser emission could be used as the zero reference because no change in setup would be required. Following the laser specs in Section 3.2.1 and assuming a 10 °C temperature swing, the maximum drift would only be 8 MHz. This maps to a tolerable 5

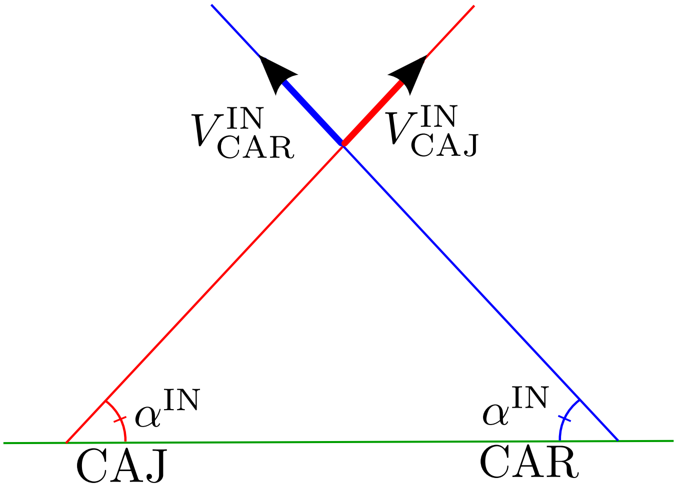

Figure 4.7: Profile view of inline viewing geometry.

m/s velocity shift calculated using Equation 3.12:

$$\Delta V^{\text{laser}} = \left(\frac{8\,\text{E}\,6}{8\,\text{E}\,6 + c/632.8\,\text{E-9}} \right) c = 5.06 \text{ m/s.} \tag{4.14}$$

The laser analysis would just take one additional step of running the laser Fourier coefficients through the LM least-squares algorithm to compute an estimate of Doppler velocity, using the same process as for the airglow coefficients. Since the laser source is not moving in the reference frame of the instrument and is close in frequency to the airglow emission, it can be used as the zero-Doppler reference. The difference between the frequency of the laser and airglow emission needs to be accounted for because it puts the laser fringe at a much different order than the emission spectrum. Using the Doppler shift equation (Equation 3.12), the velocity offset from laser to airglow wavelengths can be calculated:

$$V^{\text{offset}} = \left(\frac{632.8\,\text{E-9} - 630\,\text{E-9}}{630\,\text{E-9}} \right) c = 1.332\,\text{E}\,6 \text{ m/s.} \tag{4.15}$$

This offset will be subtracted from all $V_i^{\text{laser}}(t)$ terms so the velocities will all be in the correct reference wavelength. The laser Doppler velocity will be interpolated across the entire night to get the Doppler offset, $\hat{\beta}_i(t) = V_i^{\text{laser}}(t) - V^{\text{offset}}$, in Equation 4.4. With this extra variable known, no assumptions have to be made when estimating zenith or inline velocities. The vertical winds can then be solved to be

$$\hat{w}^{\mathrm{IN}} = \frac{V_{\mathrm{CAJ}}^{\mathrm{IN}} - \tilde{\hat{\beta}}_{\mathrm{CAJ}} + V_{\mathrm{CAR}}^{\mathrm{IN}} - \tilde{\hat{\beta}}_{\mathrm{CAR}}}{2\sin(\alpha^{\mathrm{IN}})} \tag{4.16}$$

$$\hat{w}_i^{\mathrm{zenith}} = V_i^{\mathrm{zenith}} - \tilde{\hat{\beta}}_i. \tag{4.17}$$

The newly estimated vertical winds must then be interpolated across the entire night for use in estimating the absolute Doppler shifts of the other LOS measurements. These interpolated vertical wind estimates, along with the interpolated laser velocity, reduces the unknowns and, thus, cardinal and horizontal common volume winds can be calculated. Cardinal winds can be calculated as

$$\hat{x} = (V_i^{\mathrm{cardinal}} - \tilde{\hat{w}}\sin(\alpha_i) - \tilde{\hat{\beta}}_i)/\cos(\alpha_i). \tag{4.18}$$

Like the zero-zenith method, the common volume measurements can be set up in matrix form and solved for zonal and meridional winds:

$$\hat{u} = \frac{V_{\mathrm{CAJ}}^{\mathrm{H}}\cos(\theta_{\mathrm{CAR}}) - V_{\mathrm{CAR}}^{\mathrm{H}}\cos(\theta_{\mathrm{CAJ}})}{\sin(\theta_{\mathrm{CAJ}} - \theta_{\mathrm{CAR}})} \tag{4.19}$$

$$\hat{v} = \frac{V_{\mathrm{CAJ}}^{\mathrm{H}}\sin(\theta_{\mathrm{CAR}}) - V_{\mathrm{CAR}}^{\mathrm{H}}\sin(\theta_{\mathrm{CAJ}})}{\sin(\theta_{\mathrm{CAR}} - \theta_{\mathrm{CAJ}})} \tag{4.20}$$

where the horizontal components are

$$V_{\mathrm{CAJ}}^{\mathrm{H}} = \frac{V_{\mathrm{CAJ}}^{\mathrm{LOS}} - \tilde{\hat{w}}\sin(\alpha_{\mathrm{CAJ}}) - \tilde{\hat{\beta}}_{\mathrm{CAJ}}}{\cos(\alpha_{\mathrm{CAJ}})} \tag{4.21}$$

$$V_{\mathrm{CAR}}^{\mathrm{H}} = \frac{V_{\mathrm{CAR}}^{\mathrm{LOS}} - \tilde{\hat{w}}\sin(\alpha_{\mathrm{CAR}}) - \tilde{\hat{\beta}}_{\mathrm{CAR}}}{\cos(\alpha_{\mathrm{CAR}})}. \tag{4.22}$$

Figure 4.8 shows a typical night's wavelength shifted laser velocity compared to the airglow LOS zenith velocity. Note that this "corrected" velocity is still far off from being a good zero reference (but it is much better than it was; see Figure 4.2). This difference is likely due to the laser not being locked to exactly 632.8 nm. In fact, post analysis calculations show the laser wavelength to be approximately 632.78964 nm. To get the correct β term from the laser, unfortunately another zenith wind assumption is made — the average vertical wind velocity over a single night is zero — and instead of subtracting the constant from Equation 4.15, the laser Doppler must be fit to

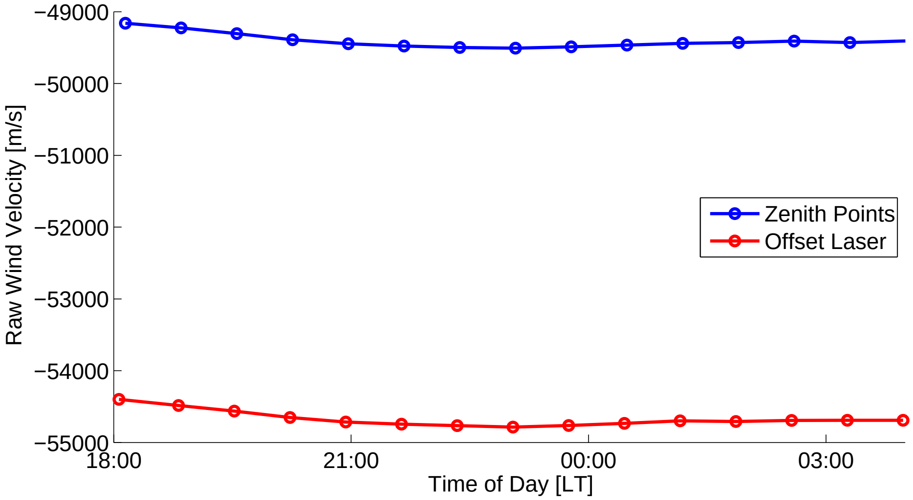

Figure 4.8: An entire night's wavelength corrected laser and raw zenith velocities taken from the LM analysis of the second fringe on November 7-8, 2010 at Cariri.

the 630.0-nm emission zenith LOS Doppler profile. Although vertical winds may exist throughout the night, averaging across the whole night should give an average-zero vertical wind. This is an improved assumption (in comparison to assuming that the vertical wind is zero at all times) because it allows for vertical winds to exist under the constraint that they average out to zero, making it less stringent than the previous assumption. A best-fit spline is used to map the laser to the zenith velocity between the hours of 21:00 and 04:00 local time. These hours were chosen because they avoid dawn and dusk when other factors may cause large vertical winds and low airglow intensities, which can cause high uncertainties. This laser profile offset by the zero-average vertical wind assumption is compared to the raw zenith winds in Figure 4.9. Now, $\hat{\beta}_i(t) = V_i^{\text{laser}}(t) - \hat{V}_i^{\text{fit offset}}$, which can be interpolated and used in Equations 4.19 and 4.20 to analyze the same night's data and compute neutral winds.

Figure 4.10 shows the zero-laser techniques results; note how all the winds become more self-consistent when compared to Figure 4.6. Not only are the three independent vertical measurements in better agreement (and show a clear post-sunset downward wind), but the meridional and zonal winds from the two common volume points also match better. Although there is close agreement, the stability of the laser may still be questionable and false winds

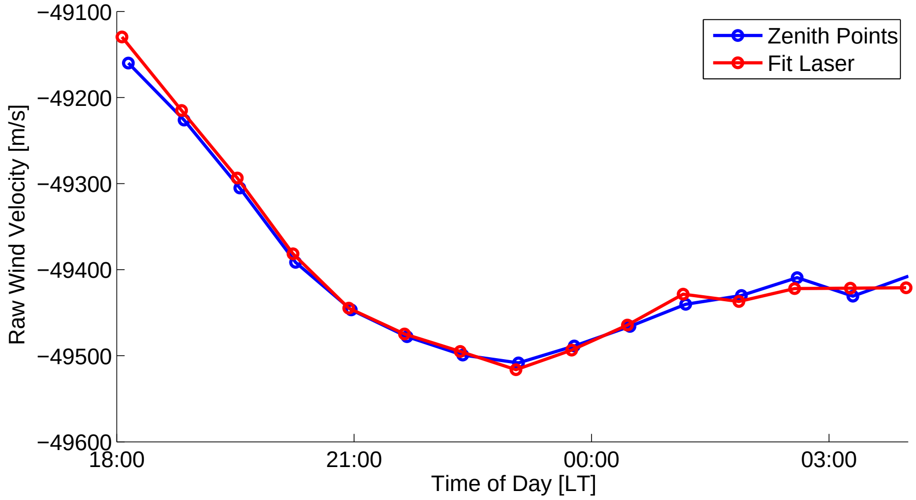

Figure 4.9: An entire night's laser observations fit to zero-averaged zenith observations taken from the LM analysis of the second fringe on November 7-8, 2010 at Cariri.

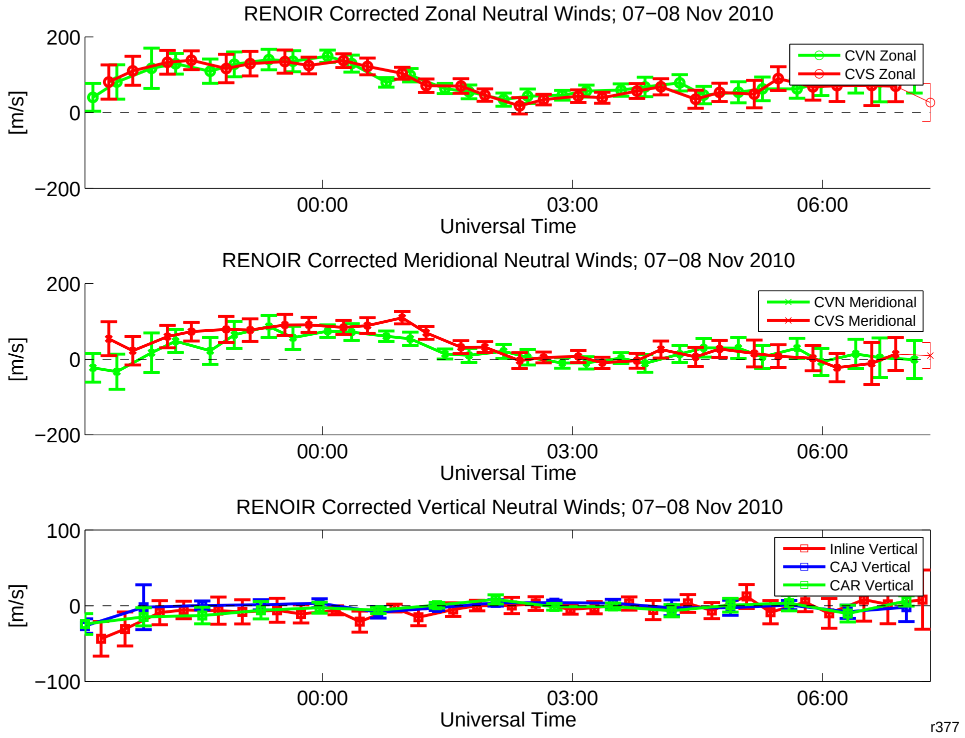

Figure 4.10: Common volume winds analyzed using zero-laser technique on November 7-8, 2010.

could possibly be obtained. The effects of drifts in the laser frequency will be studied in Chapter 5.

4.2.3 Zero-Lamp Technique

Although using the laser was an attempt to remove a priori assumptions, one still had to be made on vertical winds in the thermosphere; and even though this condition is looser than the zero-zenith assumption, it would be good to have a better method for determining the Doppler zero reference. Although it had been assumed that the HeNe laser was stable, it may in fact be mode hopping early in the evening because it is not thermally controlled, and the temperatures inside the trailer can exceed the stated working specs of the laser. Also, these temperatures are higher than the set control point for the etalon, so the gap spacing will undergo thermal expansion. This is the same time period when our supposed vertical winds are largest. Furthermore, the laser frequency is controlled by the cavity length inside the laser, which might have a temperature dependence.

An alternate emission source is that provided by a hollow cathode lamp (HCL). The emission wavelength from an HCL is set by a chemical reaction and is not expected to have a temperature dependence. Thus, we can create a zero-reference utilizing the HCL emission in the same way as we used the HeNe laser as a reference in the previous section. To test this lamp technique, a BaNe hollow cathode lamp was added to the system and imaged intermittently between the laser and airglow exposures. The cathode lamp glows due to a chemical reaction and creates a similar redline wavelength (630.479 nm); therefore, it should be a good source as a zero reference.

The same wavelength normalization issue that occurred with the laser will also happen with this lamp. The Doppler shift equation (Equation 3.12) can be used again to find the velocity offset from the lamp to airglow wavelengths:

$$V^{\text{offset}} = \left(\frac{630.479\,\text{E-9} - 630\,\text{E-9}}{630\,\text{E-9}} \right) c = 227.7\,\text{E}\,3 \text{ m/s}. \tag{4.23}$$

However, this source is not exactly at 630.479 nm (as Figure 4.11 shows, the offset from Equation 4.23 does not align to the 630.0-nm observations) so it, too, must be fit to the observations made in the zenith directions.

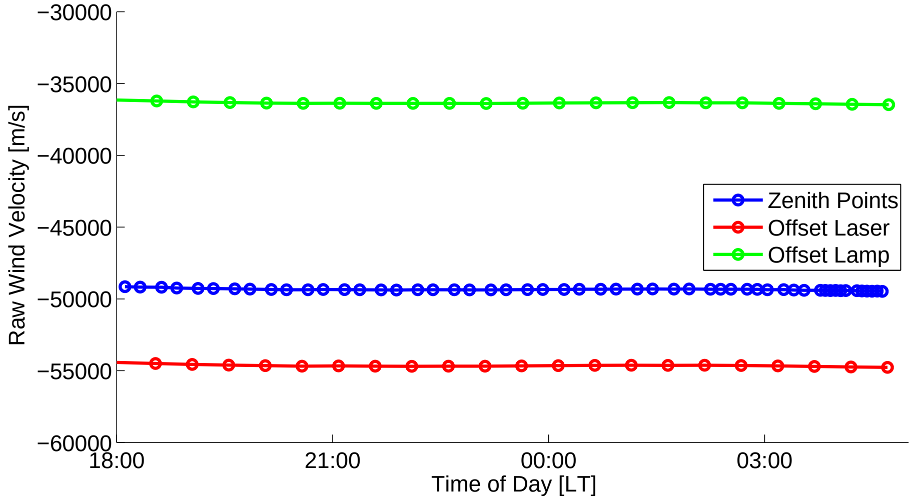

Figure 4.11: An entire night's wavelength corrected lamp, laser, and raw zenith velocities taken from the LM analysis of the second fringe on September 21-22, 2011 at Cariri.

Post analysis calculation shows the lamp wavelength to be approximately 630.50602 nm. The same assumption that the vertical wind averages to zero between 21:00 and 04:00, therefore, has to be made in order to fit the zenith observations to the lamp measurements. Thus, $\hat{\beta}_i(t) = V_i^{\text{lamp}}(t) - \hat{V}_i^{\text{fit offset}}$, which will then be interpolated to all measurement times. This $\hat{\beta}_i$ derived from the lamp will be used just like the $\hat{\beta}_i$ derived from the laser; it will be used in Equations 4.16 and 4.17 to find the vertical wind component and Equations 4.19 and 4.20 to find the horizontal wind components. Figure 4.12 shows that the lamp, laser, and zenith measurements all show reasonable agreement. Figure 4.13 shows the zenith wind estimates obtained using the three different zero-Doppler reference techniques described here. This figure shows that, while all are similar in uncertainties for most of the night, there are some discrepancies between the HeNe- and HCL-derived vertical winds. Chapter 5 will investigate why the two methods are not in agreement as well as attempt to verify the vertical winds.

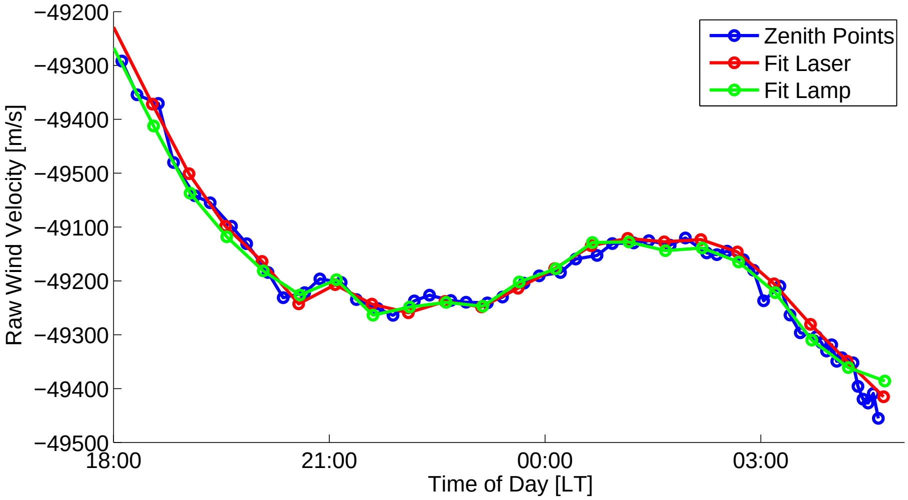

Figure 4.12: An entire night's lamp and laser observations fit to zero-averaged zenith observations taken from the LM analysis of the second fringe on September 21-22, 2011 at Cariri. The shifted fit makes the average zero zenith wind assumption between 21:00 and 04:00 LT.

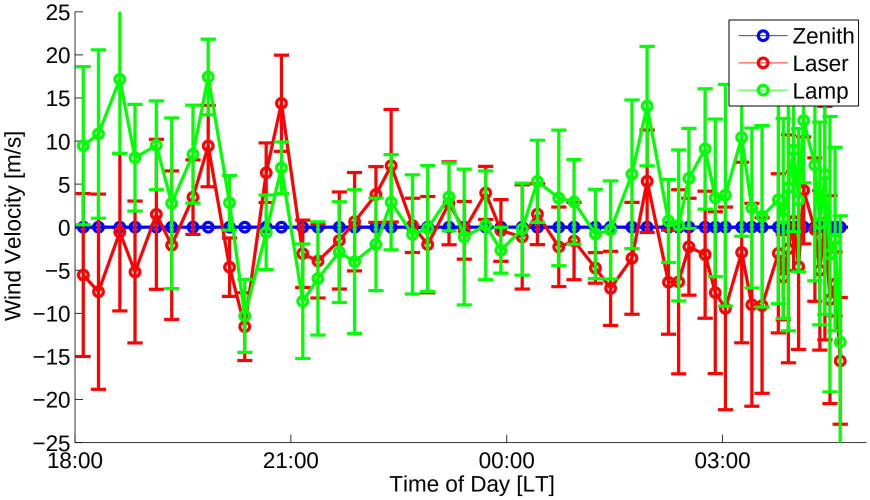

Figure 4.13: Zenith winds analyzed using zero-lamp technique compared to other techniques on September 21-22, 2011 at Cariri.

CHAPTER 5

RESULTS AND DISCUSSION

The following chapter aims to demonstrate that the zero-laser technique is sufficient in wind analysis and that vertical winds are actually seen in Brazil in the local summer months.

5.1 Simulation

In order to investigate how vertical winds would propagate through our analysis of the line-of-sight Doppler velocities, a series of simulations were run. Starting with Equation 4.4 and a set wind field (u, v, w), all the Doppler velocity equations can be calculated as in Chapter 4. However, if we treat β as the combination of the reference offset and reference error, we can then investigate how errors in this reference will propagate into the vertical and horizontal wind directions. Let the total Doppler offset be the combination of the correct instrument reference factor plus a possible error term: $\hat{\beta}_i = \beta_i + \beta_i^{\text{error}}$.

First, we begin by comparing the errors in three vertical winds with the errors in reference. Assuming the reference correction term correctly maps the zero-Doppler velocity at the laser wavelength to the zero-Doppler velocity at 630.0 nm and there is no laser drift, $\beta_i^{\text{error}} = 0$ for all sites. With no reference error, Equations 4.16 and 4.17 will produce equivalent vertical wind speeds at all three zenith points: Cajazeiras, Cariri, and inline ($\hat{w}_{\text{CAJ}}^{\text{zenith}} = \hat{w}_{\text{CAR}}^{\text{zenith}} = \hat{w}^{\text{IN}} = w$). Thus, with no error, a correct vertical wind is seen in agreement at all three locations.

Now letting β_i^{error} be non-zero, we cannot be sure that our result is from an actual vertical wind or an artifact of having a poor Doppler reference; mathematically, $\hat{w} = w + \epsilon_w$. We can simulate what the vertical wind estimation error, ϵ_w, will be for a range of laser reference errors, β^{error}, in order to see what artificial winds could be produced:

$$\epsilon_{w^{\mathrm{IN}}} = \frac{-\beta_{\mathrm{CAJ}}^{\mathrm{error}} - \beta_{\mathrm{CAR}}^{\mathrm{error}}}{2\sin(\alpha_{\mathrm{IN}})} \tag{5.1}$$

$$\epsilon_{w_i^{\mathrm{Z}}} = -\beta_i^{\mathrm{error}}. \tag{5.2}$$

Note that these results have a geometry dependence specific to our system. Figure 5.1 plots these equations to show that all three estimation errors are nearly proportional to β^{error} when the two sites have equal errors. Since the reference error has mapped into both the inline-derived vertical wind and zenith-derived vertical winds, neither $\hat{w}^{\mathrm{IN}} = w$ nor $\hat{w}_i^{\mathrm{zenith}} = w$. The assumption is made that $\beta_{\mathrm{CAJ}}^{\mathrm{error}} \approx \beta_{\mathrm{CAR}}^{\mathrm{error}}$ so the two zenith-derived vertical winds are in agreement. This assumption may not be true, but in such a case, the three vertical wind error estimates would be inconsistent, and the reference error would be easily identifiable (see Figure 5.2). The three false vertical winds all lie within each other's errorbars (set at 5 m/s, which is typical for the observations from these instruments) when β^{error} is below 40 m/s. Since they are self-consistent and reasonable vertical velocities, a self-consistent erroneous vertical wind could be inferred from the data. This consistency check does not clarify if the resultant wind is real or not, so we must look at the horizontal wind estimates as well.

By comparing the errors in zonal and meridional winds from the north and south common volume locations, we can run a similar simulation comparing estimated wind errors by letting $\hat{u} = u + \epsilon_u$ and $\hat{v} = v + \epsilon_v$. First, let us set $\hat{w} = 0$ as was assumed in the zero-zenith technique (see Section 4.2.1). With no reference error, Equations 4.8 and 4.9 will produce equivalent horizontal wind speeds for CVN and CVS ($\hat{u}^{\mathrm{CVN}} = \hat{u}^{\mathrm{CVS}} = u$ and $\hat{v}^{\mathrm{CVN}} = \hat{v}^{\mathrm{CVS}} = v$). If a Doppler reference error is introduced, the errors in the estimated zonal and meridional winds are:

$$\epsilon_{u^{\mathrm{CV}}} = \frac{-\beta_{\mathrm{CAJ}}^{\mathrm{error}}\cos(\theta_{\mathrm{CAR}}) + \beta_{\mathrm{CAR}}^{\mathrm{error}}\cos(\theta_{\mathrm{CAJ}})}{\cos(\alpha^{\mathrm{CV}})\sin(\theta_{\mathrm{CAJ}} - \theta_{\mathrm{CAR}})} \tag{5.3}$$

$$\epsilon_{v^{\mathrm{CV}}} = \frac{-\beta_{\mathrm{CAJ}}^{\mathrm{error}}\sin(\theta_{\mathrm{CAR}}) + \beta_{\mathrm{CAR}}^{\mathrm{error}}\sin(\theta_{\mathrm{CAJ}})}{\cos(\alpha^{\mathrm{CV}})\sin(\theta_{\mathrm{CAR}} - \theta_{\mathrm{CAJ}})}. \tag{5.4}$$

Figure 5.3 shows how the errors estimated in both zonal and meridional directions diverge with increasing reference error, unlike the vertical winds.

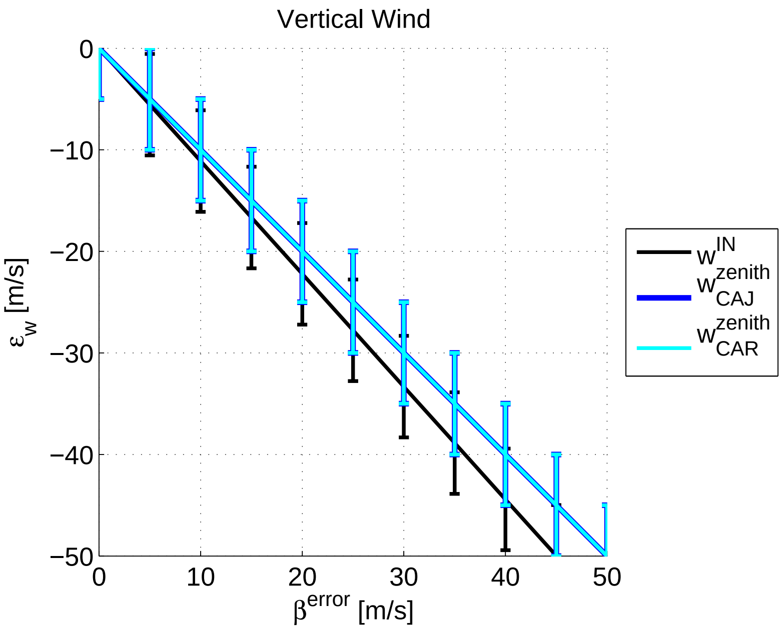

Figure 5.1: Vertical wind error (comparing inline and zenith observation directions) with equal errors in each reference.

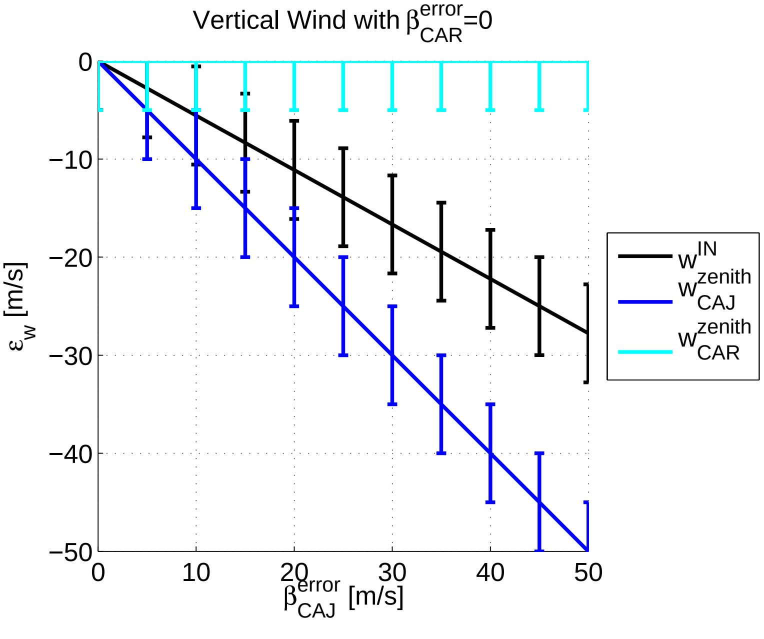

Figure 5.2: Vertical wind error (comparing inline and zenith observation directions) with unequal errors in reference.

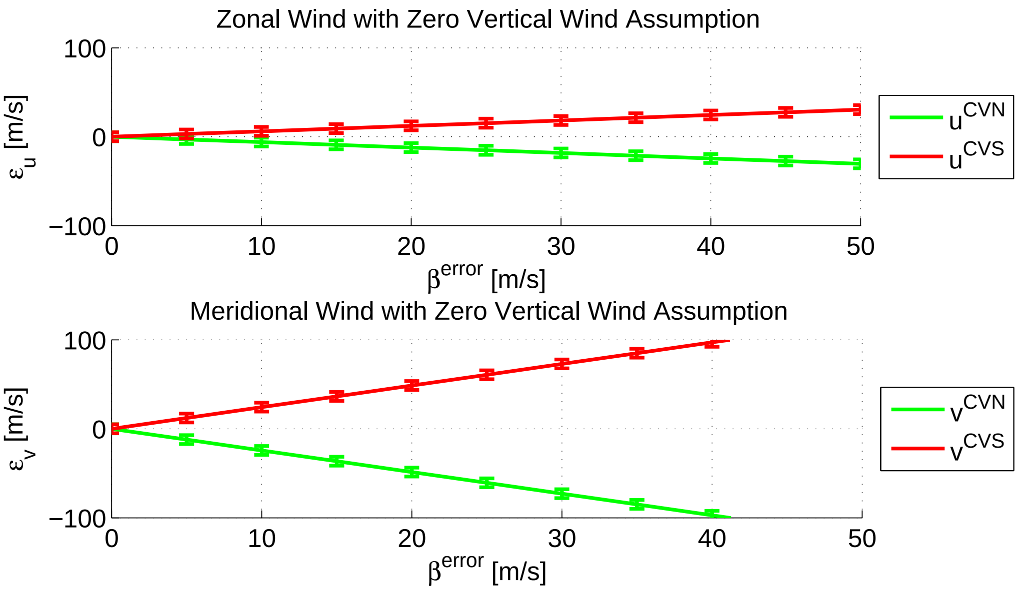

Figure 5.3: Horizontal wind errors comparing CVN and CVS with a range of erroneous Doppler references assuming no vertical wind.

Note here that the divergence in the meridional direction is roughly four times greater than in the zonal direction due to RENOIR's geometry, as seen in Figure 3.7. In such a small region, the horizontal winds should be fairly comparable, and gradients of 200 m/s over 300 km are not reasonable during most conditions. Physically, if such a divergence actually occurred, there must be vertical motion of neutral particles, or a vacuum would form in this region. While this horizontal wind error comparison does not confirm or deny the existence of vertical winds in the data, it does suggest that setting the vertical winds to zero across the entire night is a poor assumption.

Now, let the vertical wind be some non-zero value estimated from observations made towards the zenith direction, $\hat{w} = V_i^{\text{zenith}} + \hat{\beta}_i$, as in the zero-laser technique (see Section 4.2.2). This $\hat{\beta}_i$ is composed of the reference offset plus an error term that has to be factored into the horizontal wind error calculations. Again, with no reference error, Equations 4.19 and 4.20 will produce equivalent horizontal wind speeds at CVN and CVS ($\hat{u}^{\text{CVN}} = \hat{u}^{\text{CVS}} = u$ and $\hat{v}^{\text{CVN}} = \hat{v}^{\text{CVS}} = v$). If a Doppler reference error is introduced, the errors in

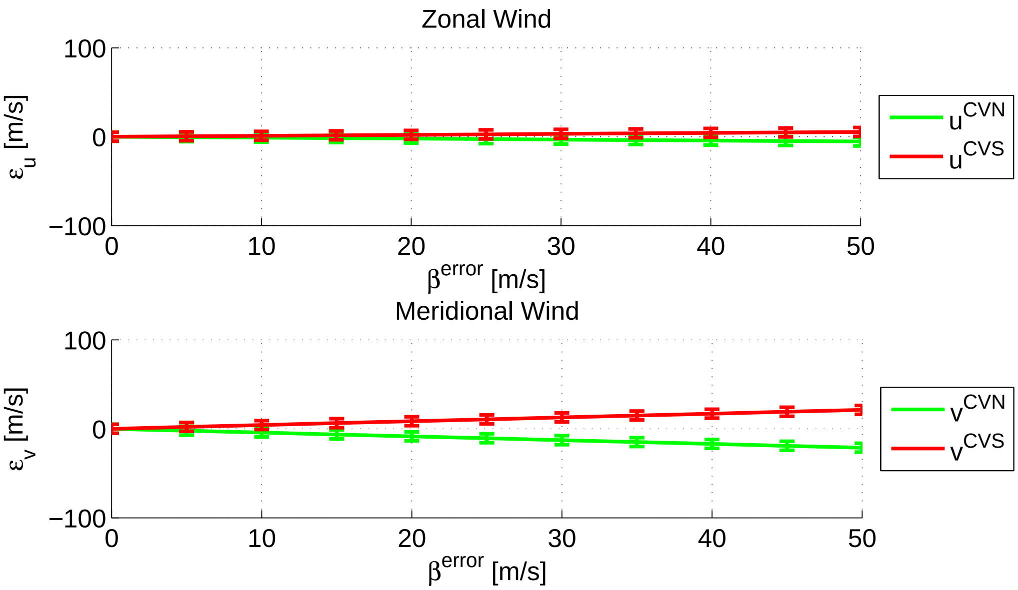

Figure 5.4: Horizontal wind errors comparing CVN and CVS with various errors in reference.

the estimated zonal and meridional winds are:

$$\epsilon_{u^{\text{CV}}} = \frac{-\beta^{\text{error}}_{\text{CAJ}}(1-\sin(\alpha^{\text{CV}}))\cos(\theta_{\text{CAR}}) + \beta^{\text{error}}_{\text{CAR}}(1-\sin(\alpha^{\text{CV}}))\cos(\theta_{\text{CAJ}})}{\cos(\alpha^{\text{CV}})\sin(\theta_{\text{CAJ}}-\theta_{\text{CAR}})} \tag{5.5}$$

$$\epsilon_{v^{\text{CV}}} = \frac{-\beta^{\text{error}}_{\text{CAJ}}(1-\sin(\alpha^{\text{CV}}))\sin(\theta_{\text{CAR}}) + \beta^{\text{error}}_{\text{CAR}}(1-\sin(\alpha^{\text{CV}}))\sin(\theta_{\text{CAJ}})}{\cos(\alpha^{\text{CV}})\sin(\theta_{\text{CAR}}-\theta_{\text{CAJ}})}. \tag{5.6}$$

Figure 5.4 shows how the errors in both zonal and meridional directions still diverge with increasing reference error. However, the errors are greatly reduced (by a factor of six) from those seen in Figure 5.3. This error reduction confirms that the large discrepancies in horizontal winds are due to the incorrect assumption that the vertical winds are always zero, because β^{error} has absorbed this vertical wind error. While gradients of 30 m/s over 300 km are plausible in the thermosphere, it would seem highly unreasonable to get β^{error} much greater than 5 m/s. The maximum drift expected in the laser, according to the datasheet, is 5.06 m/s (calculated in Equation 4.14). With reference errors less than 10 m/s, the error bars of the two meridional estimates overlap, as do the two estimates for zonal wind and the three estimates of vertical wind. Since these are all in good agreement, our model indicates that a real downward 40 m/s wind is outside the range of possible reference error induced winds. While the simulations did not help prove the existence of vertical winds, they did verify the ability to correctly observe vertical winds if the system is running within the stated instrument specifications. This simulation also helps justify the use of the zero-laser technique over the zero-zenith technique because it removes unrealistic meridional and zonal velocity gradients.

5.2 Results

We utilize data collected during the first three years of observations in Brazil; during two of these years, the instruments ran in common volume mode when both sites were operational. This plethora of data has been analyzed with both the zero-zenith and the zero-laser techniques in order to show the improvements of the zero-laser method over the zero-zenith method in so much as to have renamed the zero-zenith processing "uncorrected" and the zero-laser processing "corrected".

In order to demonstrate this point, a few nights of observations obtained in CV mode from 2010 and 2011 are presented in Figures 5.5 to 5.16. Both the uncorrected (using the zero-zenith technique) and corrected (using the zero-laser technique) results are shown for comparison. It is immediately apparent that the uncertainties in the wind estimates have increased from zero-zenith to zero-laser. This increase is because the laser and zenith variances must be incorporated into the LOS variances since they are both used to deduce the horizontal component wind. Examining the horizontal velocities, we see that the winds calculated under the assumption of zero-vertical wind are not usually self-consistent while the winds calculated using the zero-laser technique are. Note that, for each of the nights presented in Figures 5.5 to 5.10, a downward wind of nearly -40 m/s is seen at dusk while the vertical wind is approximately 0 m/s for the rest of the night. The second point to note is the difference between the meridional winds at the two CV locations during dusk. The zero-zenith analysis has a $\sim$200 m/s divergence while the zero-laser analysis shows that the meridional winds at the two locations are in much closer agreement. This pattern is in line with what is seen from the simulated results presented in Figures 5.3 and 5.4; using the zero-zenith reference and forcing the vertical wind to zero maps the actual vertical winds into the reference error and creates the 200 m/s divergence. On the other hand, using the zero-laser reference allows a vertical wind to exist. Using this estimated vertical wind in the analysis of the CV data reduces the discrepancies between the north and south CV estimates. Comparing the figures of all uncorrected nights with corrected nights shows that the divergences seen in the meridional winds are all greatly reduced when the zero-laser technique is used. Furthermore, these large divergences are present in the uncorrected nights only when vertical winds are present.

The large downward winds in the dusk sector are only seen in the data during the local summer months (November through February). By stacking each day's estimated vertical winds, this trend can be seen in Figure 5.17. Since this effect is only seen in the summer, changes in the laser stability and etalon gap in changing thermal conditions could be causing these estimated vertical winds at dusk, because the trailers get extremely hot during the day and take time to cool off. More testing is still needed because the thermal environment may exceed both the set temperature of the thermally controlled encasing of the etalon and the laser's operational temperature. If these temperatures are outside of the instrument specifications, β^{error} may drift in excess of the estimated 5 m/s, causing an increase in the estimated vertical wind error. The laser's possible thermal dependence is why the temperature invariant hollow cathode lamp (HCL) was added for comparison with the laser technique. Figure 5.18 compares a single night's laser-reference and lamp-reference deduced zenith velocities and overlays the measured trailer temperature. While the temperature sensor used to make this measurement is not calibrated, it can still show how the relative temperature compares to the estimated winds; neither appears to follow the ambient temperature. However, there are a few discrepancies between vertical wind estimates that must be explained. Figure 5.19 shows the relative change in the output of the LM temperature estimate for both the laser and lamp and compares them with the trailer temperature. The LM outputs are not actual temperatures but rather estimates of the width of the fringe over the night. While the laser's "temperature" is relatively constant, the HCL's temperature fluctuates with the temperature in the trailer across the entire night. It is likely that if the changing ambient temperature affects the lamp temperature estimates, it also affects the lamp Doppler estimates and could explain the discrepancies between lamp and laser zenith estimates. Therefore, the zero-laser technique is still being used to analyse the Brazilian FPI data. The improvements seen in the analyzed data, both in allowing vertical winds and reducing the meridional wind divergence between common volume measurement points, are sufficient to justify its use as the “correct” Doppler-reference technique.

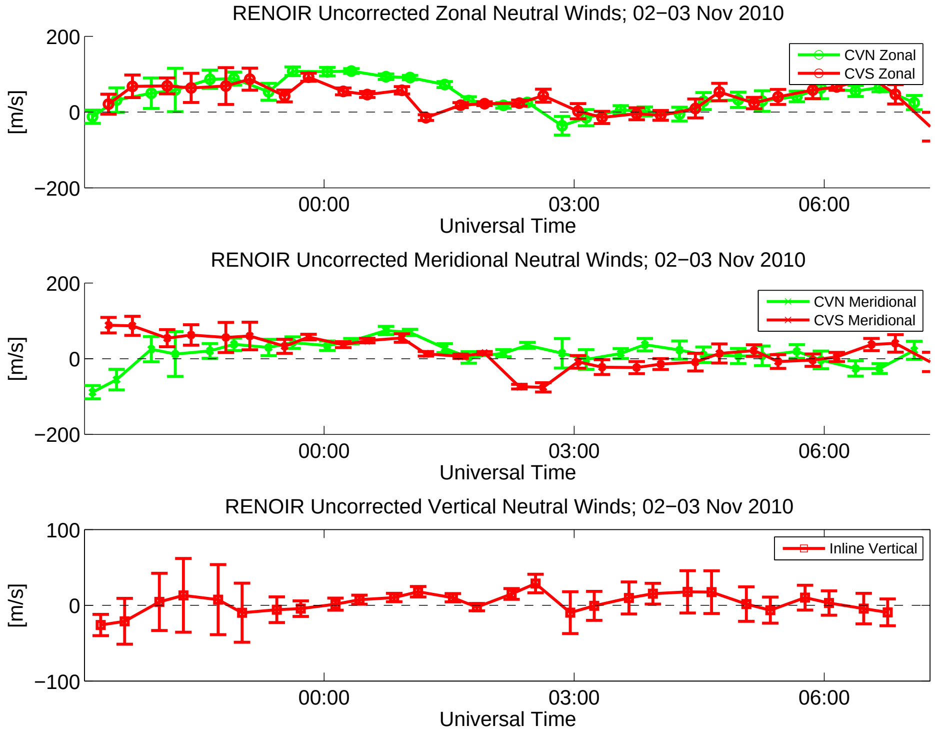

Figure 5.5: November 2-3, 2010 winds derived with zero-zenith technique.

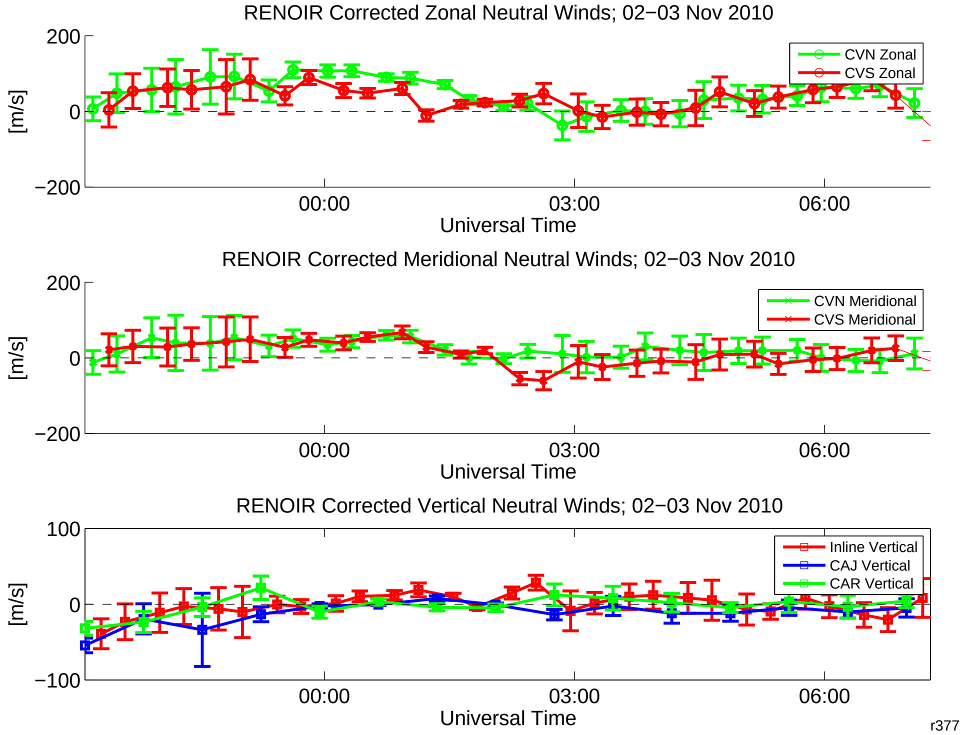

Figure 5.6: November 2-3, 2010 winds derived with zero-laser technique.

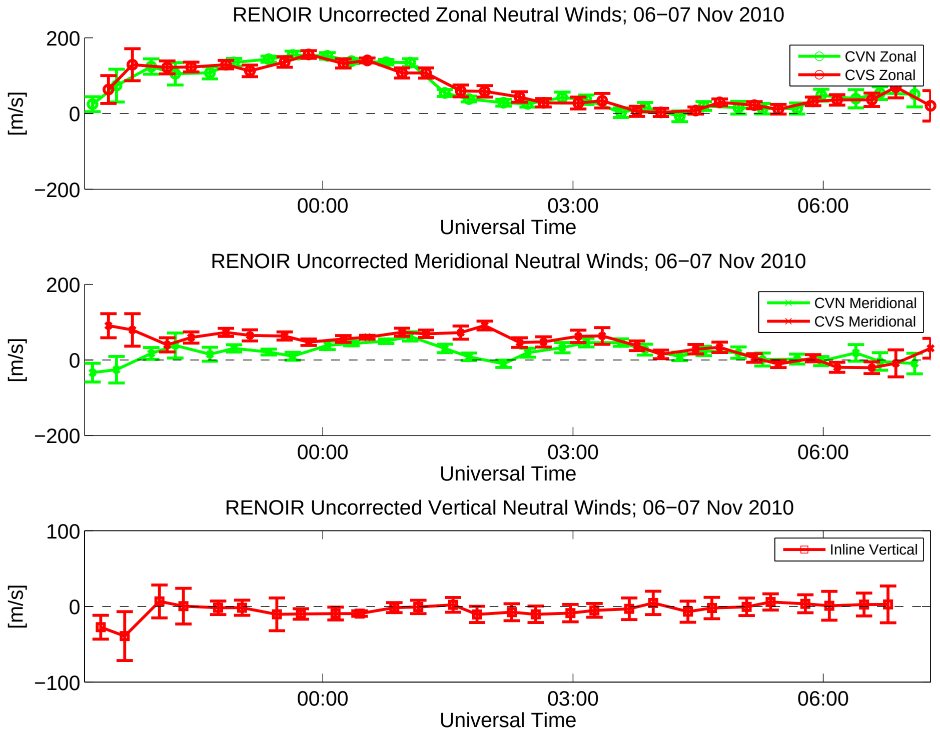

Figure 5.7: November 6-7, 2010 winds derived with zero-zenith technique.

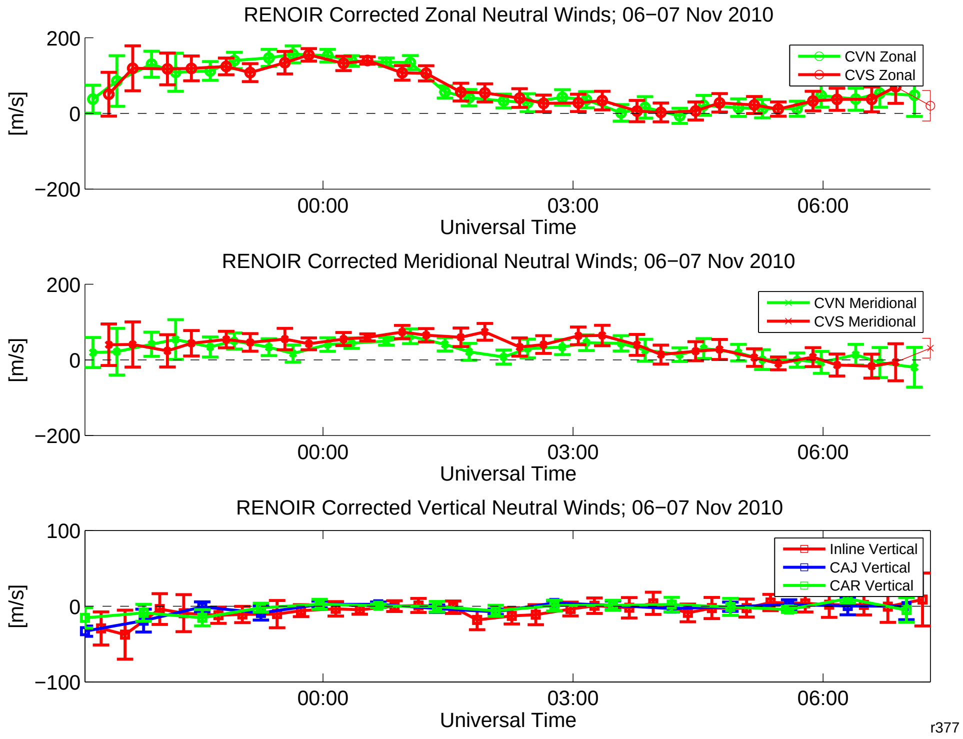

Figure 5.8: November 6-7, 2010 winds derived with zero-laser technique.

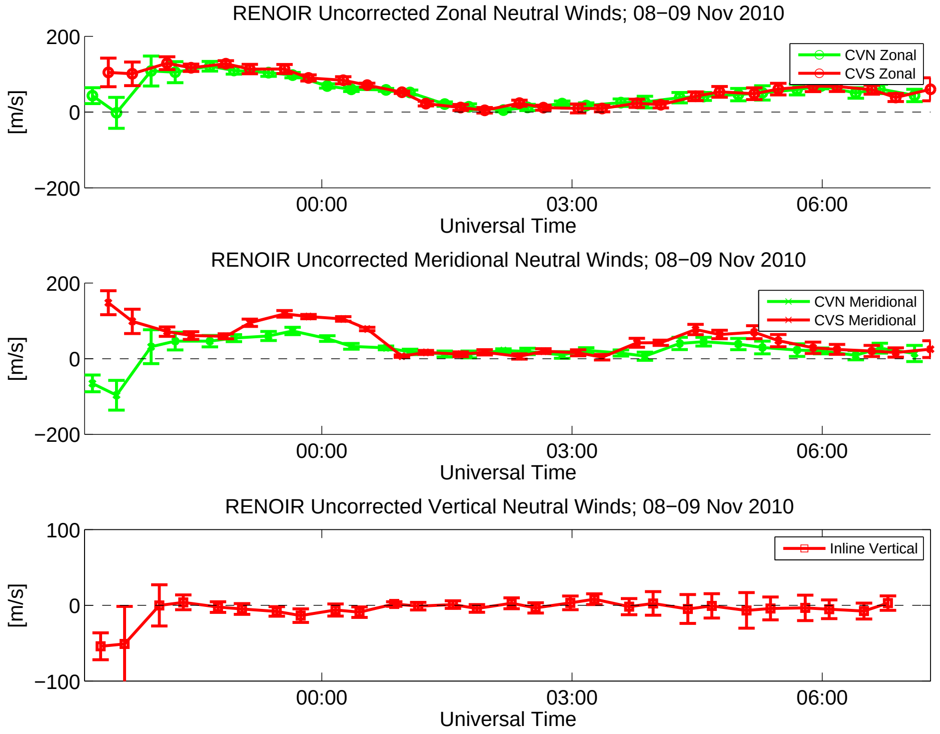
RENOIR Uncorrected Zonal Neutral Winds; 08−09 Nov 2010

RENOIR Uncorrected Meridional Neutral Winds; 08−09 Nov 2010

RENOIR Uncorrected Vertical Neutral Winds; 08−09 Nov 2010

Figure 5.9: November 8-9, 2010 winds derived with zero-zenith technique.

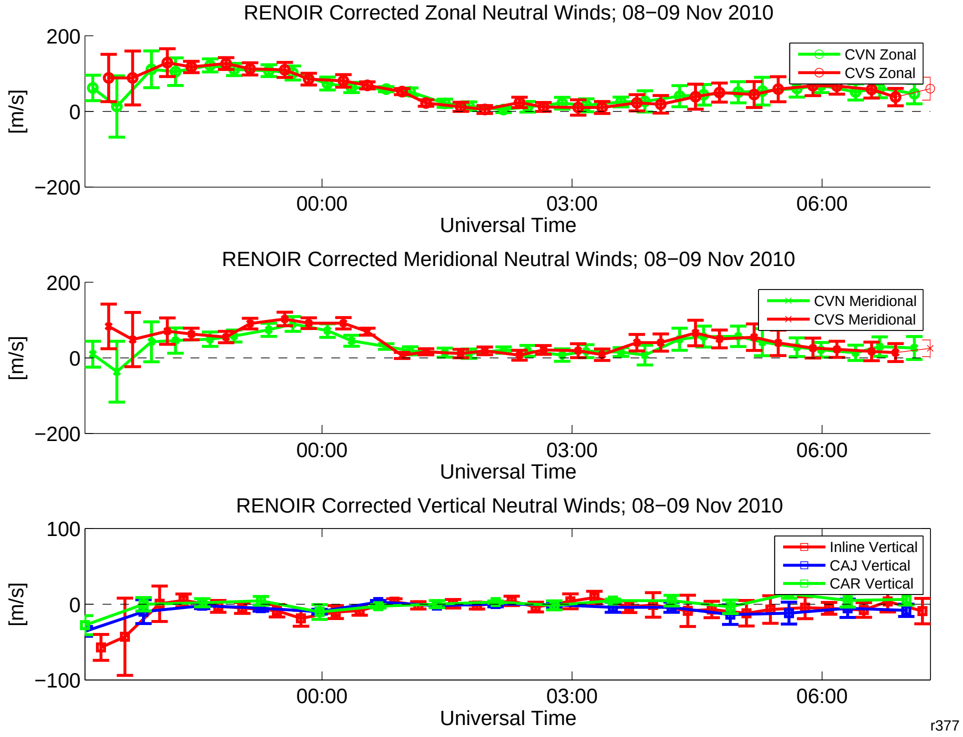
RENOIR Corrected Zonal Neutral Winds; 08−09 Nov 2010

RENOIR Corrected Meridional Neutral Winds; 08−09 Nov 2010

RENOIR Corrected Vertical Neutral Winds; 08−09 Nov 2010

Figure 5.10: November 8-9, 2010 winds derived with zero-laser technique.

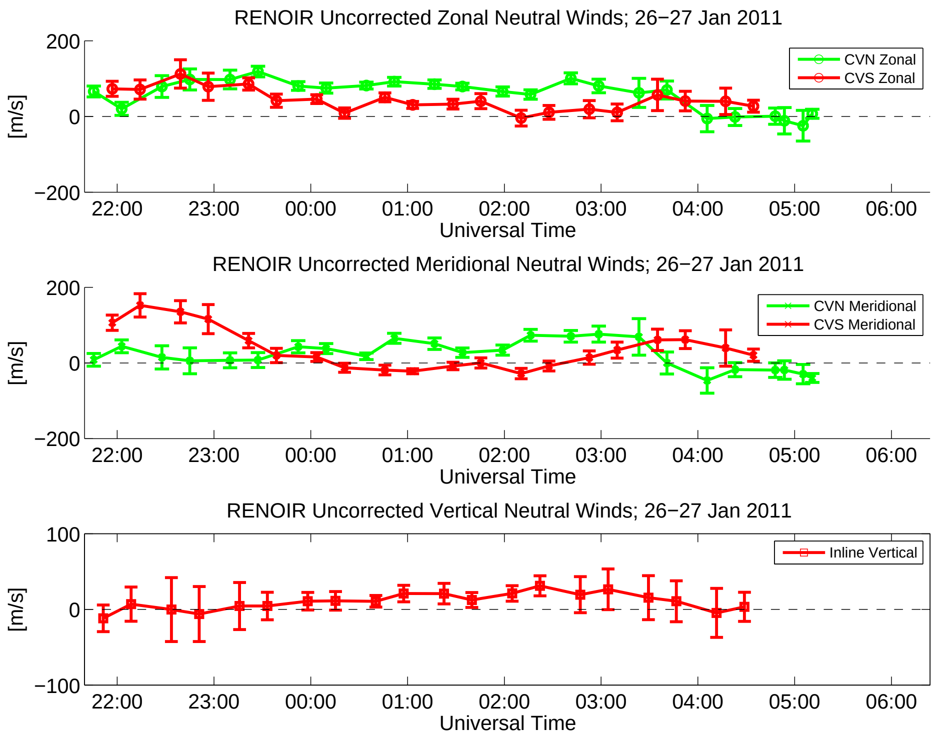

Figure 5.11: January 26-27, 2011 winds derived with zero-zenith technique.

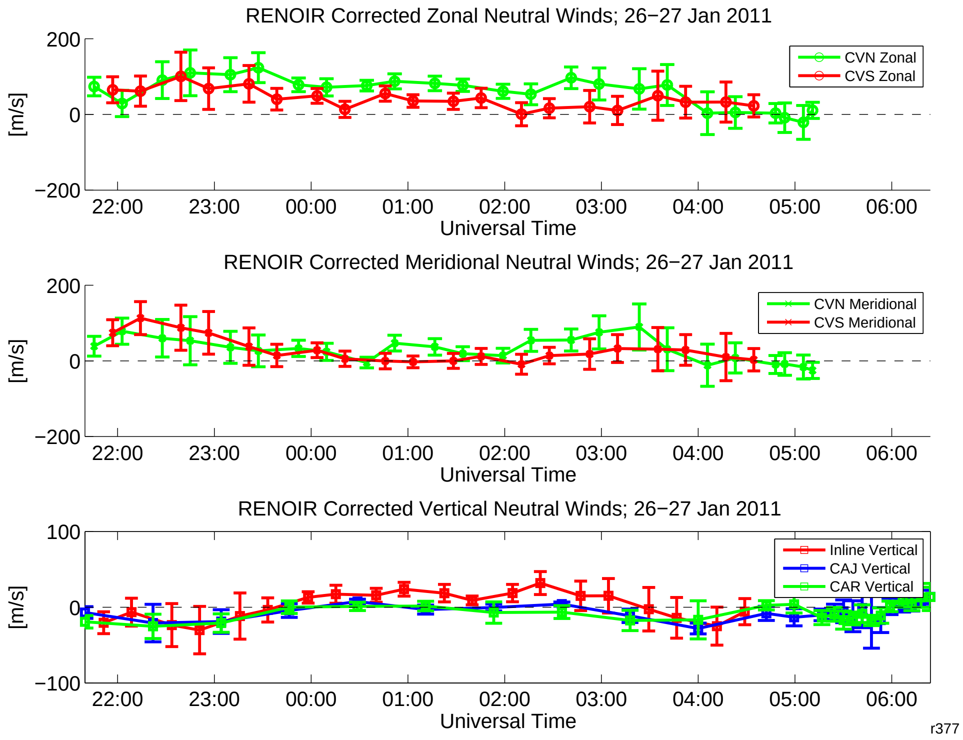

Figure 5.12: January 26-27, 2011 winds derived with zero-laser technique.

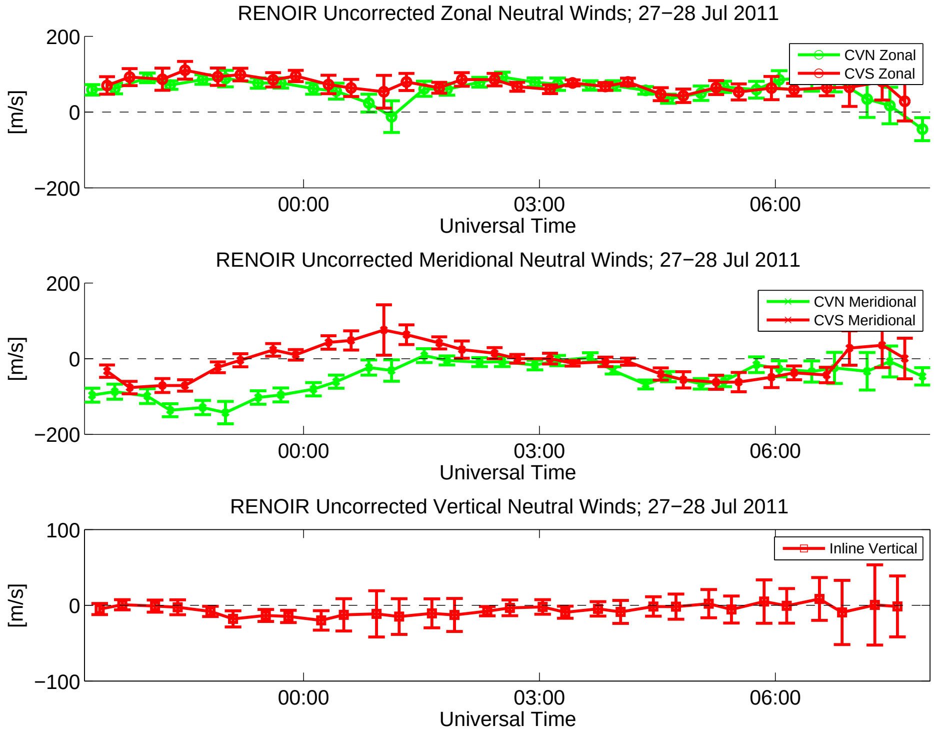

Figure 5.13: July 27-28, 2011 winds derived with zero-zenith technique.

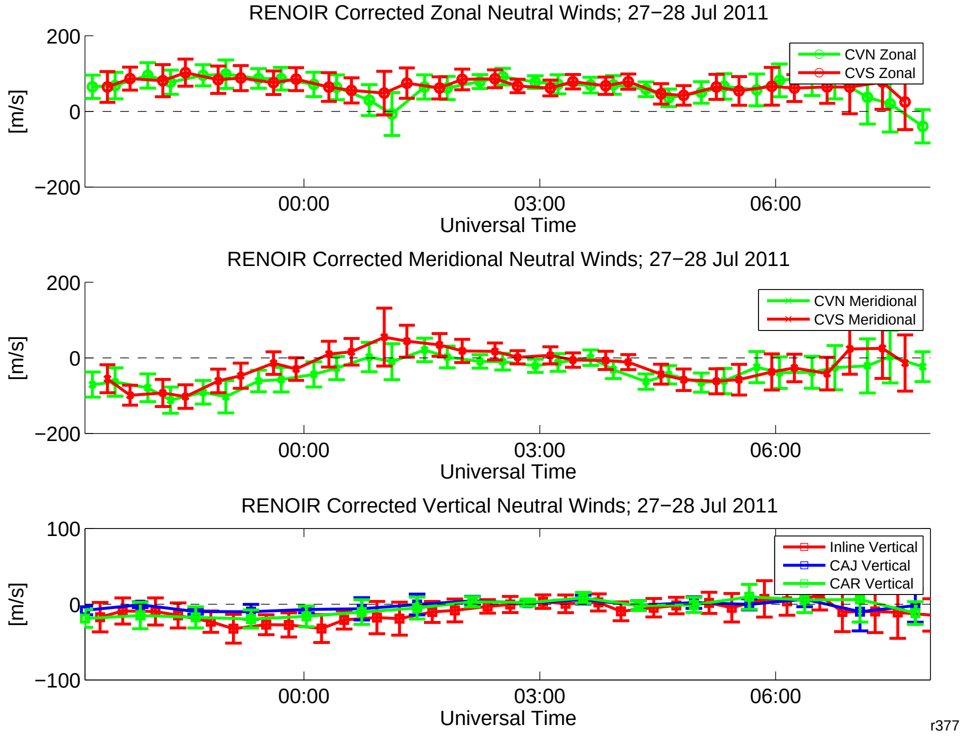

Figure 5.14: July 27-28, 2011 winds derived with zero-laser technique.

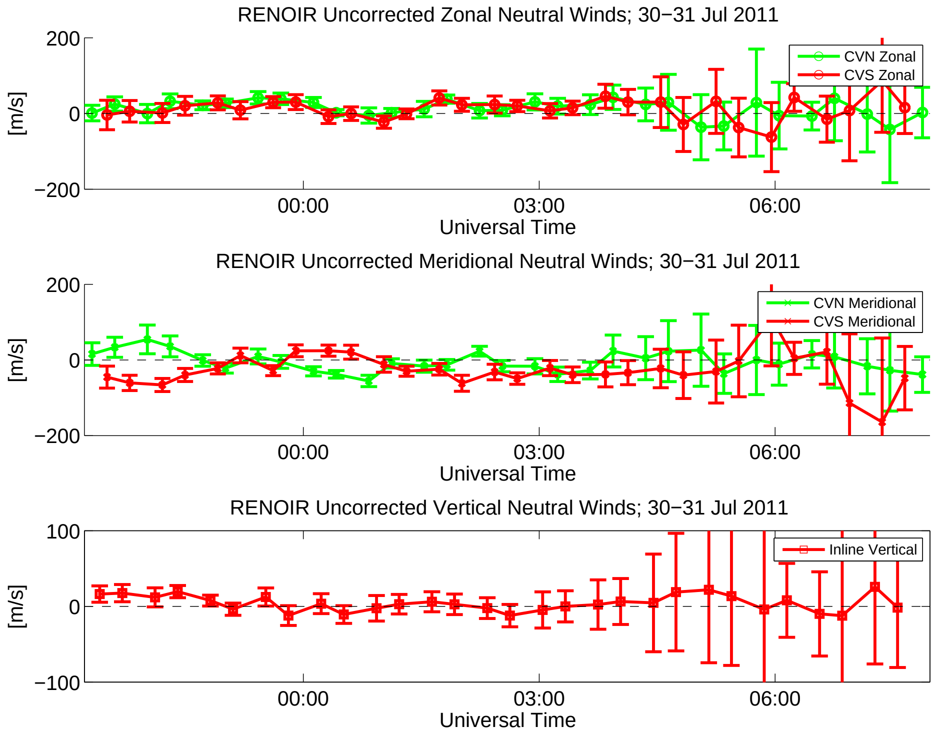

Figure 5.15: July 30-31, 2011 winds derived with zero-zenith technique.

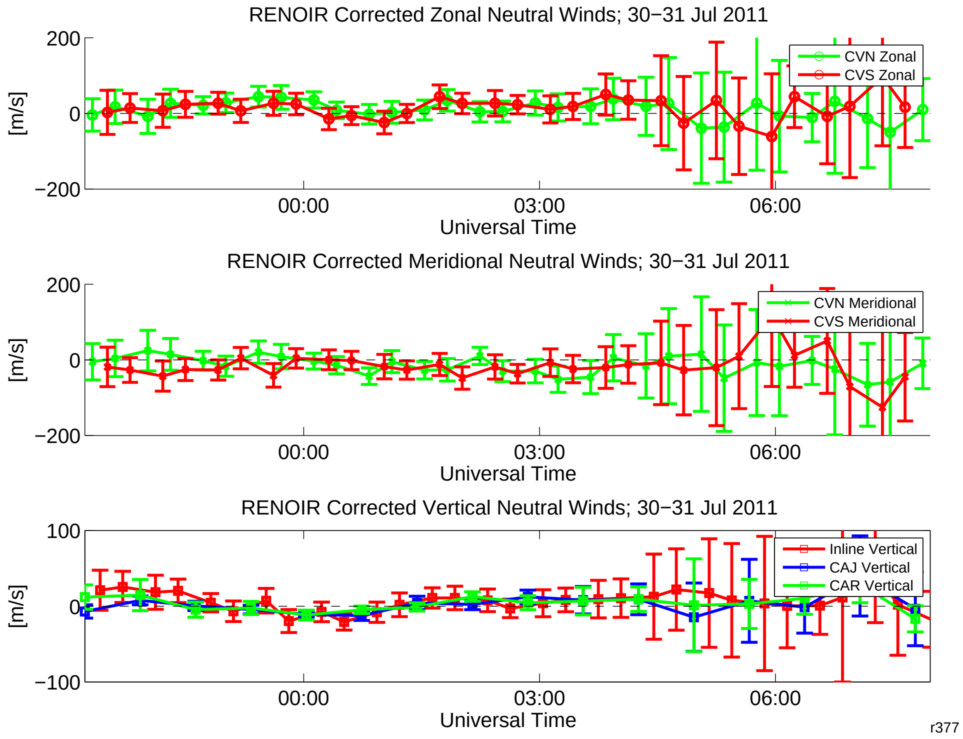

Figure 5.16: July 30-31, 2011 winds derived with zero-laser technique.

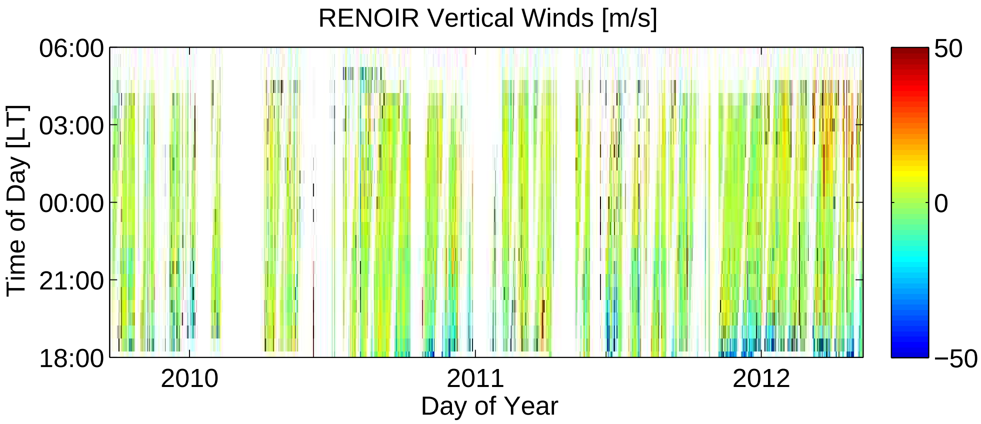

Figure 5.17: Vertical winds collected from Brazil from late 2009 to early 2012.

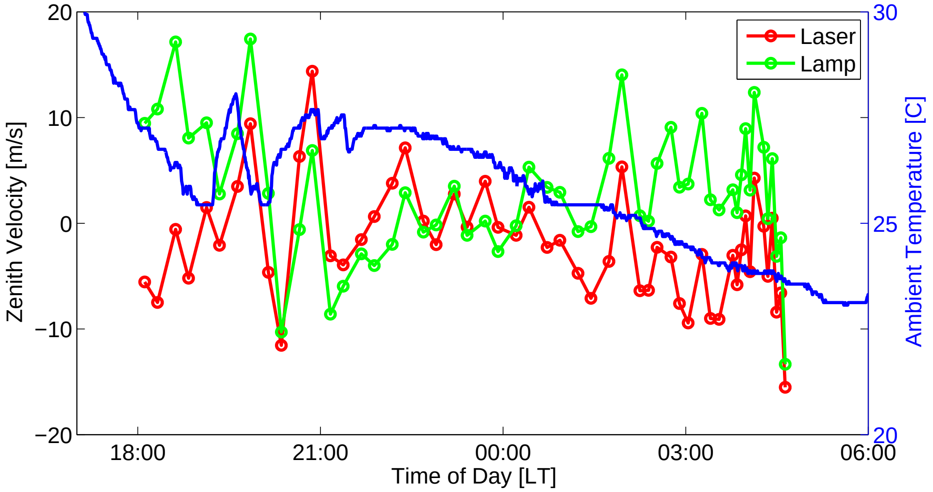

Figure 5.18: Zenith winds analyzed using zero-laser and zero-lamp techniques compared to ambient temperature on September 21-22, 2011 at Cariri.

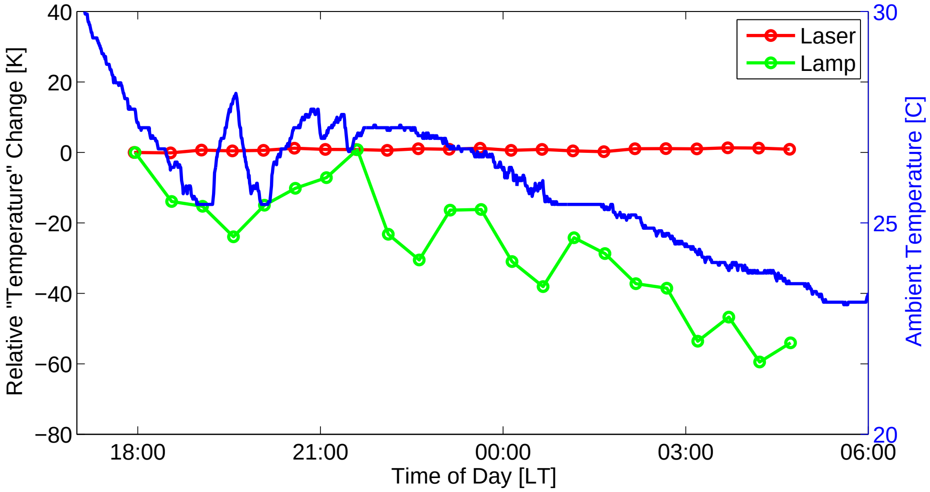

Figure 5.19: Relative “temperature” change of the laser and lamp from LM estimation compared to ambient temperature on September 21-22, 2011 at Cariri.

CHAPTER 6

CONCLUSION

6.1 Conclusions

This thesis develops a new technique to establish a zero-Doppler reference for FPI measurements of the thermospheric neutral winds by employing observations of a frequency-stabilized HeNe laser. The newly established zero-laser technique is designed to analyze the recent data obtained in RENOIR's new common volume mode utilizing the already imaged laser at each site. The reference offset is computed using previously established methods for airglow Doppler velocity estimation; the offset is necessary in estimating the vector horizontal winds as well as estimating the vertical winds both from zenith and inline measurements. This new method greatly improves the agreement of the meridional winds from the two common volume points in our RENOIR data and relaxes the zero-vertical wind assumption.

In Chapter 2, an introduction to the upper atmosphere is given. A description of the coincident neutral atmosphere and ionosphere is also covered. The composition of these regions has been discussed, touching on how the chemical reactions of their constituents create the 630.0-nm airglow emission. The F-region dynamo is then described, explaining how upper atmosphere winds are driven and their role in driving commonly measured electron/ion drifts. After describing typical thermospheric temperatures, the history of FPI use in airglow measurements takes us to the current RENOIR project in Brazil.

In Chapter 3, an overview of the Fabry-Perot interferometer and RENOIR system parameters is given. First, the basic fringe pattern is derived from first-order principles. Useful parameters to describe the physical workings of the etalon are then covered, including how Doppler measurements are made. Then, the two Brazilian field sites are detailed along with the setup of the instrumentation there. Finally, the different viewing geometry modes of the system are discussed.

In Chapter 4, a breakdown of the analysis and the zero-Doppler techniques is given. First, there is an overview of the steps taken to convert an FPI image into an estimate of Doppler velocity. Then, the equations for converting LOS Doppler velocities to geographic winds are defined. Finally, each of the three techniques — zero-zenith, zero-laser, and zero-lamp — is clarified to explain each's assumptions and how the component wind vectors are derived.

In Chapter 5, a comparison of both simulations and actual results using the Doppler techniques is given. A mathematical simulation of error propagation is first covered for the zenith and laser zero-Doppler methods. Then, a few samples of results show the improvement in horizontal and vertical wind agreement from CVN, CVS, and inline observation directions. The zero-laser technique is finally chosen as the best choice for analysis.

6.2 Future Work

Although the laser method is chosen as the best zero-Doppler technique, further testing still needs to be performed. The existence of the summer vertical winds is still debatable since the laser stability in different temperature conditions is, as of yet, unknown. In-lab experiments that categorize the precise response of the laser to different temperatures and temperature gradients should be looked at thoroughly. Now that solar maximum is approaching, airglow intensities are increasing and less exposure time is needed for a single observation. Shorter exposures allow the possibility of higher-resolution temporal sampling, which could be used to run curl and divergence tests. Such tests provide another means to estimate vertical winds because of the assumption of incompressible flow; wind fields must be divergence free (or the earth's atmosphere would disappear), so estimates of horizontal divergence can lead to estimates of vertical motion.

Colleagues have created a 2D FPI analysis routine that analyzes the whole image without compressing it into a 1D fringe [27]. This implementation also has the advantage of estimating etalon parameters over the course of the night. Rerunning RENIOR data through this algorithm could further improve the data quality as well as determine if etalon or laser effects are causing the vertical winds we see. Quantitatively comparing the 1D and 2D methods would be the next important step in our FPI analysis.

Currently, four FPIs are deployed across the United States in a specific chained geometry that gives good north-south and east-west spatial coverage of the mid-latitude ionosphere [28]. This setup, named the North American Thermosphere Ionopshere Observing Network (NATION), provides more common volume points of comparison and, in the future, a tri-static observation point. Although this experiment is being conducted at a different latitude, all the analysis techniques developed in this thesis can be applied. Reference error simulations could be done with all possible common volume pairs, and vertical wind patterns could also be studied from these sites. Another good test of the vertical wind calculations that can currently be done would be to compare two sites that have an inline point directly over a third site. This experiment would provide two independent observations of vertical wind at the same time and location, an improvement over RENOIR's three independent vertical measurements taken at different times and locations. Additionally, the numerous sites could take measurements to do a curl and divergence analysis of the wind field. The new data from this experiment, much like the RENOIR data, will be crucial to enhancing and possibly even correcting current neutral wind models and increasing our understanding of the physics of the upper atmosphere.

REFERENCES

[1] M. Biondi, “Measured vertical motion and converging and diverging horizontal flow of the midlatitude thermosphere,” *Geophysical Research Letters*, vol. 11, no. 1, pp. 84–87, Jan. 1984. [Online]. Available: http://doi.wiley.com/10.1029/GL011i001p00084

[2] M. Biondi and D. Sipler, “Horizontal and vertical winds and temperatures in the equatorial thermosphere: Measurements from Natal, Brazil during August–September 1982,” *Planetary and Space Science*, vol. 33, no. 7, pp. 817–823, July 1985. [Online]. Available: http://linkinghub.elsevier.com/retrieve/pii/0032063385900352

[3] B. Anandarao, R. Raghavarao, J. Desai, and G. Haerendel, “Vertical winds and turbulence over Thumba,” *Journal of Atmospheric and Terrestrial Physics*, vol. 40, no. 2, pp. 157–163, Feb. 1978. [Online]. Available: http://linkinghub.elsevier.com/retrieve/pii/002191697890020X

[4] R. Raghavarao, W. Hoegy, N. Spencer, and L. Wharton, “Neutral temperature anomaly in the equatorial thermosphere-A source of vertical winds,” *Geophysical Research Letters*, vol. 20, no. 11, pp. 1023–1026, June 1993. [Online]. Available: http://doi.wiley.com/10.1029/93GL01253

[5] A. Hedin, J. Salah, J. Evans, C. Reber, G. Newton, N. Spencer, D. Kayser, D. Alcaydé, P. Bauer, L. Cogger, and J. McClure, “A global thermospheric model based on mass spectrometer and incoherent scatter data MSIS, 1. N_2 density and temperature,” *Journal of Geophysical Research*, vol. 82, no. 16, pp. 2139–2147, June 1977. [Online]. Available: http://doi.wiley.com/10.1029/JA082i016p02139

[6] A. Hedin, N. Spencer, and T. Killeen, “Empirical global model of upper thermosphere winds based on Atmosphere and Dynamics Explorer satellite data,” *Journal of Geophysical Research*, vol. 93, no. A9, p. 9959, 1988. [Online]. Available: http://doi.wiley.com/10.1029/JA093iA09p09959

[7] R. Akmaev, T. Fuller-Rowell, F. Wu, J. Forbes, X. Zhang, A. Anghel, M. Iredell, S. Moorthi, and H.-M. Juang, "Tidal variability in the lower thermosphere: Comparison of Whole Atmosphere Model (WAM) simulations with observations from TIMED," *Geophysical Research Letters*, vol. 35, no. 3, p. L03810, Feb. 2008. [Online]. Available: http://doi.wiley.com/10.1029/2007GL032584

[8] D. Drob, J. Emmert, G. Crowley, J. Picone, G. Shepherd, W. Skinner, P. Hays, R. Niciejewski, M. Larsen, C. She, J. Meriwether, G. Hernandez, M. Jarvis, D. Sipler, C. Tepley, M. O'Brien, J. Bowman, Q. Wu, Y. Murayama, S. Kawamura, I. Reid, and R. Vincent, "An empirical model of the Earth's horizontal wind fields: HWM07," *Journal of Geophysical Research*, vol. 113, no. A12, pp. 1–18, Dec. 2008. [Online]. Available: http://www.agu.org/pubs/crossref/2008/2008JA013668.shtml

[9] M. C. Kelley, *The Earth's Ionosphere.* Burlington, MA: Academic Press, 1989.

[10] G. Herzberg, *Atomic Spectra and Atomic Structure.* New York, NY: Dover Publications, 1944.

[11] R. A. Craig, *The Upper Atmosphere Meteorology and Physics.* New York, NY: Academic Press, 1965.

[12] H. Rishbeth and O. Garriott, *Introduction to Ionospheric Physics.* New York, NY: Academic Press, 1969.

[13] P. Hays, D. Rusch, R. Roble, and J. Walker, "The OI (6300 Å) airglow," *Reviews of Geophysics and Space Physics*, vol. 16, no. 2, p. 225, 1978. [Online]. Available: http://www.agu.org/pubs/crossref/1978/RG016i002p00225.shtml

[14] R. Link and L. Cogger, "A reexamination of the OI 6300-Å nightglow," *Journal of Geophysical Research*, vol. 93, no. A9, p. 9883, 1988. [Online]. Available: http://doi.wiley.com/10.1029/JA093iA09p09883

[15] H. Rishbeth, "The equatorial F-layer: progress and puzzles," *Annales Geophysicae*, vol. 18, no. 7, pp. 730–739, July 2000. [Online]. Available: http://www.springerlink.com/index/GH791560JVX07157.pdf

[16] A. Hedin, E. Fleming, A. Manson, F. Schmidlin, S. Avery, R. Clark, S. Franke, G. Fraser, T. Tsuda, F. Vial, and R. Vincent, "Empirical wind model for the upper, middle and lower atmosphere," *Journal of Atmospheric and Terrestrial Physics*, vol. 58, no. 13, pp. 1421–1447, Sep. 1996. [Online]. Available: http://linkinghub.elsevier.com/retrieve/pii/0021916995001220

[17] J. Mariska and L. Oster, "Solar activity and the variations of the geomagnetic K_p-index," *Solar Physics*, vol. 26, no. 1, pp. 241–249, Sep. 1972. [Online]. Available: http://adsabs.harvard.edu/full/1972BAAS....4R.389O http://link.springer.com/10.1007/BF00155123

[18] F. Herrero, H. Mayr, and N. Spencer, "Latitudinal (seasonal) variations in the thermospheric midnight temperature maximum: A tidal analysis," *Journal of Geophysical Research*, vol. 88, no. A9, p. 7225, 1983. [Online]. Available: http://doi.wiley.com/10.1029/JA088iA09p07225

[19] J. Meriwether, J. Makela, Y. Huang, D. Fisher, R. Buriti, A. Medeiros, and H. Takahashi, "Climatology of the nighttime equatorial thermospheric winds and temperatures over Brazil near solar minimum," *Journal of Geophysical Research*, vol. 116, no. A4, p. A04322, Apr. 2011. [Online]. Available: http://doi.wiley.com/10.1029/2011JA016477

[20] H. Babcock, "A Study of the green auroral line by the interference method," *The Astrophysical Journal*, vol. 57, p. 209, May 1923. [Online]. Available: http://adsabs.harvard.edu/doi/10.1086/142747

[21] G. Hernandez and R. Roble, "Direct measurements of nighttime thermospheric winds and temperatures, 1. Seasonal variations during geomagnetic quiet periods," *Journal of Geophysical Research*, vol. 81, no. 13, p. 2065, 1976. [Online]. Available: http://www.agu.org/pubs/crossref/1976/JA081i013p02065.shtml

[22] R. Dickinson and J. Geisler, "Vertical motion field in the middle thermosphere from satellite drag densities," *Monthly Weather Review*, vol. 96, no. 9, pp. 606–616, 1968. [Online]. Available: http://docs.lib.noaa.gov/rescue/mwr/096/mwr-096-09-0606.pdf

[23] A. Richmond, E. Ridley, and R. Roble, "A thermosphere/ionosphere general circulation model with coupled electrodynamics," *Geophysical Research Letters*, vol. 19, no. 6, pp. 601–604, Mar. 1992. [Online]. Available: http://www.athena-spu.gr/ftp/lfsc/Literature/Roble_1988_TGCM.pdf http://doi.wiley.com/10.1029/92GL00401

[24] J. Vaughan, *The Fabry-Perot Interferometer*. Philadelphia, PA: IOP Publishing, 1989.

[25] J. Makela, J. Meriwether, Y. Huang, and P. Sherwood, "Simulation and analysis of a multi-order imaging Fabry-Perot interferometer for the study of thermospheric winds and temperatures," *Applied Optics*, vol. 50, no. 22, p. 4403, July 2011. [Online]. Available: http://www.opticsinfobase.org/abstract.cfm?URI=ao-50-22-4403

[26] T. Killeen and P. Hays, “Doppler line profile analysis for a multichannel Fabry-Perot interferometer,” *Applied Optics*, vol. 23, no. 4, p. 612, Feb. 1984. [Online]. Available: http://www.opticsinfobase.org/abstract.cfm?URI=ao-23-4-612

[27] M. Conde, “Deriving wavelength spectra from fringe images from a fixed-gap single-etalon Fabry-Perot spectrometer,” *Applied Optics*, vol. 41, no. 14, pp. 2672–8, May 2002. [Online]. Available: http://www.opticsinfobase.org/abstract.cfm?URI=ao-41-14-2672

[28] J. Makela, J. Meriwether, A. Ridley, M. Ciocca, and M. Castellez, “Large-scale measurements of thermospheric dynamics with a multisite Fabry-Perot interferometer network: Overview of plans and results from midlatitude measurements,” *International Journal of Geophysics*, vol. 2012, no. 3, pp. 1–10, 2012. [Online]. Available: http://www.hindawi.com/journals/ijgp/2012/872140/